NAVAL POSTGRADUATE SCHOOL

MONTEREY, CALIFORNIA

THESIS

SUPER-RADIANT FREE ELECTRON LASER MEASUREMENT AND DETECTION

by

Conor Michael Pogue

September 2013

Thesis Co Advisors:	William Colson
	Keith Cohn
Second Reader:	Joe Blau

Approved for public release; distribution is unlimited

THIS PAGE INTENTIONALLY LEFT BLANK

A free electron laser (FEL) is a type of laser that use relativistic electron bunches and a periodic magnetic field to generate coherent radiation. These types of lasers are of interest to the Navy because they can operate at the high average power with excellent optical beam quality that is needed in many military applications. A current project between the U.S. Navy and Niowave Inc. is to create a super-radiant FEL that uses superconducting spoke cavities for the electron accelerating structures. These types of cavities have never been used in an FEL before and may be more suitable for deployment on naval platforms due to their smaller size and structural rigidity compared to more conventional cavities. Furthermore, spoke cavities allow operation at lower accelerating frequencies while still maintaining reasonable size cavities, which may reduce power requirements for the cryoplant. This thesis will discuss variety of optical transport and detection arrangements for various setups and FEL operational regimes.

i

THIS PAGE INTENTIONALLY LEFT BLANK

SUPER-RADIANT FREE ELECTRON LASER MEASUREMENT AND DETECTION

Conor Michael Pogue
Civilian, Naval Postgraduate School
B.S. University of California Santa Barbara, 2010

Submitted in partial fulfillment of the
requirements for the degree of

MASTER OF SCIENCE IN APPLIED PHYSICS

from the

NAVAL POSTGRADUATE SCHOOL
September 2013

Author: Conor Michael Pogue

Approved by: William B. Colson
                    Thesis Co-Advisor

                    Keith Cohn
                    Thesis Co-Advisor

                    Joe Blau
                    Thesis Second Reader

                    Andrés Larraza
                    Chair, Department of Physics

iii

THIS PAGE INTENTIONALLY LEFT BLANK

ABSTRACT

A free electron laser (FEL) is a type of laser that use relativistic electron bunches and a periodic magnetic field to generate coherent radiation. These types of lasers are of interest to the Navy because they can operate at the high average power with excellent optical beam quality that is needed in many military applications. A current project between the U.S. Navy and Niowave Inc. is to create a super-radiant FEL that uses superconducting spoke cavities for the electron accelerating structures. These types of cavities have never been used in an FEL before and may be more suitable for deployment on naval platforms due to their smaller size and structural rigidity compared to more conventional cavities. Furthermore, spoke cavities allow operation at lower accelerating frequencies while still maintaining reasonable size cavities, which may reduce power requirements for the cryoplant. This thesis will discuss variety of optical transport and detection arrangements for various setups and FEL operational regimes.

THIS PAGE INTENTIONALLY LEFT BLANK

TABLE OF CONTENTS

THIS PAGE INTENTIONALLY LEFT BLANK

LIST OF FIGURES

LIST OF TABLES

THIS PAGE INTENTIONALLY LEFT BLANK

LIST OF ACRONYMS AND ABBREVIATIONS

cm   Centimeter

DC   Direct Current

EM   Electromagnetic

FEL   Free Electron Laser

FTIR   Fourier Transform Infrared Spectroscopy

Hz   Hertz

KeV   Kilo-Electron-Volt

kHz   Kilo-Hertz

LIA   Lock-In Amplifier

nC   Nano-Coulomb

nW   Nano-Watt

MeV   Mega-Electron-Volt

mm   Milli-Meter

mrad   Milli-Radian

mV   Milli-Volt

mW   Milli-Watt

μm   Micro-Meter

μV   Micro-Volt

OAP   Off-Axis Parabolic

pC   Pico-Coulomb

ps   Picosecond

QCL   Quantum Cascade Laser

RF   Radio Frequency

THz   Tera-Hertz

UVFS   Ultra Violet grade Fused Silica

ACKNOWLEDGMENTS

I would like to first thank Prof. Bill Colson, Prof. Keith Cohn, and Prof. Joe Blau and all members of the FEL group at the Naval Postgraduate School for their help and support in this endeavor.

Secondly, I would like to thank Dr. Terry Grimm, Dr. Chase Boulwar, and all the people at Niowave Inc. during this work.

Finally, I would like to thank my parents, Ed and Bernadette, and my brother, Edward, for their words of encouragement.

THIS PAGE INTENTIONALLY LEFT BLANK

I. INTRODUCTION

A. NIOWAVE SUPER-RADIANT FEL

The U.S. Navy is currently funding Niowave Inc. to build a super-radiant free electron laser (FEL). One purpose of this project is to explore new accelerator technologies—specifically, superconducting spoke cavities—as one of the components of an FEL. Superconducting spoke cavities may be more suitable to deployment on a naval platform due to their smaller size, structural rigidity compared to more conventional cavities, ability to operate at low radio frequencies (RF), and possibly requiring only 4K refrigeration. A picture of a three spoke cavity is seen in Figure 1.

Figure 1.   Cutaway of three spoke cavity. From [1]

The spoke cavity shown has four sections where the electron beam can be accelerated by the RF fields. In between the four sections are three spoke sections that shield the electron bunches from the RF fields when the fields are in the wrong direction. The structural rigidity is aided by the spoke cavity design requiring a diameter nearly half as large as that of an elliptical accelerating cavity for the same accelerating frequency [2].

An FEL is a type of laser that uses relativistic electron bunches and an undulator (a periodic magnetic field that causes the electrons to oscillate back and forth) to generate

the coherent radiation. These types of lasers are of interest to the Navy because they have the potential to operate at high average power with excellent laser beam quality. The ability to tune the wavelength may also be important in naval applications in the maritime environment.

The Niowave FEL design uses a 5 mega-electron volt (MeV) electron beam in conjunction with a ten period variable gap undulator to generate the radiation. Varying the gap of the undulator alters the strength of the magnetic field that the electron bunches experience and changes the radiation wavelength according to Eq. (1.1):

$$\lambda \approx \frac{\lambda_o(1+K^2)}{2\gamma^2} \tag{1.1}$$

where λ_o =3.3 cm is the undulator period, $K \approx 0.1{\rightarrow}1.5$ is the undulator parameter that is proportional to the magnetic field, and γ is the Lorentz factor and is proportional to the total electron beam energy ($\gamma = E/m_e c^2$). The tunable radiation spectral range of the current Niowave FEL design will be about 150 µm to 600 µm, as the undulator gap is adjusted.

The FEL will use a thermionic cathode in conjunction with a normal conducting 350 megahertz (MHz) RF gun to generate the initial electron bunches with kinetic energies of 70 kilo-electron volts (keV). The main accelerating structure is a 700 MHz superconducting radio frequency spoke cavity that will accelerate the beam up to the final 5 MeV energy. The super-radiant FEL mechanism is largely dependent on the length of the electron bunches.

If the electron bunch meets the design requirements then the average output power of the FEL is expected to be on the order of hundreds of microwatts [3], which would be easy to detect by most far infrared and thermal detectors. If, after the accelerating process, the beam remains too long or doesn't contain enough charge, the peak current drops and the average output power can decrease by several orders of magnitude. The light generated from the FEL will propagate out from a window at the end of the beam line after the undulator. The performance of the FEL is summarized in Table 1 for a 3.5 MeV and 4 MeV electron beam.

3.5 MeV THz FEL: $\lambda \approx 310\mu m$, 350MHz, 2.7cm gap, K$\approx$0.37, N=10 periods of 3.3cm				
Pulse	q=0.2pC (70μA)	q=0.3pC (105μA)	q=0.4pC (140μA)	q=0.5pC (175μA)
Δt_b=2ps	$P_{avg}\approx48\mu W$	$P_{avg}\approx108\mu W$	$P_{avg}\approx192\mu W$	$P_{avg}\approx299\mu W$
Δt_b=4ps	$P_{avg}\approx12\mu W$	$P_{avg}\approx27\mu W$	$P_{avg}\approx48\mu W$	$P_{avg}\approx75\mu W$
Δt_b=6ps	$P_{avg}\approx5\mu W$	$P_{avg}\approx12\mu W$	$P_{avg}\approx21\mu W$	$P_{avg}\approx34\mu W$
4 MeV THz FEL: $\lambda \approx 244\mu m$, 350MHz, 2.7cm gap, K$\approx$0.37, N=10 periods of 3.3cm				
Δt_b=2ps	$P_{avg}\approx38\mu W$	$P_{avg}\approx85\mu W$	$P_{avg}\approx151\mu W$	$P_{avg}\approx237\mu W$
Δt_b=4ps	$P_{avg}\approx10\mu W$	$P_{avg}\approx21\mu W$	$P_{avg}\approx38\mu W$	$P_{avg}\approx59\mu W$
Δt_b=6ps	$P_{avg}\approx4\mu W$	$P_{avg}\approx10\mu W$	$P_{avg}\approx17\mu W$	$P_{avg}\approx26\mu W$

Table 1.   Dependence of FEL output power on beam parameters. From [3]

Table 1 shows the expected output power (P_{avg}) for various pulse lengths (Δt_b) and bunch charges (q) at two different energies (3.5 MeV and 4 MeV). In each case the undulator gap is 2.7 cm leading to an undulator parameter $K \approx 0.37$. If the parameters meet the best case scenario (q=0.5 pC and 2 ps pulse length) the output power could be ~300 µW but the worst case (q=0.2 pC and 6 ps pulse length) the output power could be on the order of 4 µW. The radiation will need to be transported from the FEL output to the diagnostic station with enough power that a detector can be used to characterize the radiation.

B.   OPTICAL BEAM TRANSPORT

The radiation generated must be transferred from the output of the FEL to the diagnostic station in order make a measurement. In the design of the transport system, the length of the transport distance, the size of the optical beam, and the wavelength need to be taken into consideration. For the experiment there will be two diagnostics that will need to be used to characterize the beam. The first is a power meter to measure the total output power. A second diagnostic is an interferometer that will be used in tandem with the power meter to reveal spectral information of the radiation produced. The latter measurement puts a requirement on the quality of the wavefronts of the radiation, as will be discussed in a subsequent chapter.

THIS PAGE INTENTIONALLY LEFT BLANK

II.   DETECTION

A.   THERMAL SENSORS

1.   Pyrometers

Pyrometers measure the energy from electromagnetic radiation by the change in temperature due to the absorption of light in the detector. The sensor material uses the pyroelectric effect to create a small voltage difference that can be measured accurately. Pyroelectricity is the generation of a voltage difference due to the change in polarization direction of a material based on a thermal gradient. It generally occurs in crystals (though it also occurs in both bone and tendon) and is closely related to piezoelectricity [4]. The electric potential difference stems from the realignment of dipoles within the material. There are two types of pyroelectricity, both of which induce a change in the polarization and create a voltage. Primary pyroelectricity occurs when the individual dipoles change length or when the randomness of the dipoles of the material is affected by the thermal gradient. Secondary pyroelectricity occurs when a thermal gradient across the crystal causes a stress or strain due to the thermal expansion of the material and the piezoelectric effect causes the realignment of the dipoles and induces the voltage difference [5]. Pyrometers do not directly detect heat, but rather detect heat flow and thus the need for a thermal gradient.

To make a sensor, the pyroelectric material is sliced into thin layers with electrodes attached on either side. A simple layout is depicted in Figure 2.
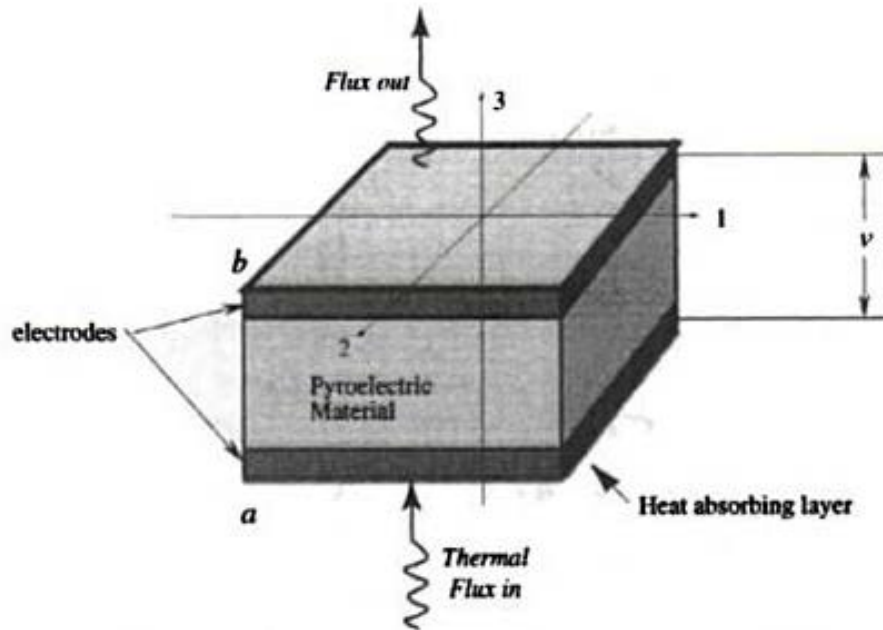
Figure 2.   Diagram of pyroelectric sensor. From [5]

On one side of the pyroelectric material is a heat absorbing layer and on the other is a heat sink.   Radiation energy is absorbed and conducts into the pyroelectric material inducing a thermal gradient in the material. The thermal gradient induces a voltage difference that can be measured by the relevant circuitry attached to the electrodes.   On the other side of material is a heat sink that allows the energy to dissipate allowing the sensor to return to its initial state.   The time constant of the detector is dependent on the speed at which the temperature of the sensor can be decreased after the thermal influx stops.   To control this, the specific heat, density and the thickness of the material can be chosen or designed accordingly.

The ability of the sensor to measure energy flux depends on the ability of the absorbing layer to take in the energy from the radiation and transfer it into thermal energy.   For this reason, pyroelectric sensors generally operate in the infrared and far-infrared region and can typically measure power levels from nW to mW scales.

2. Bolometers

a. *Room Temperature Bolometers*

Bolometers are thermal sensors that use the temperature dependence of the resistivity of a certain material to measure the absorption of electromagnetic radiation. Like pyrometers, they are used for wavelength ranges from infrared to microwave. The basic concept is that power from an electromagnetic signal is absorbed by the bolometer where it is transformed into heat. This in turn heats up a thermal mass that is connected to a heat sink at the same temperature as the ambient environment. As the heat is conducted away and dissipates, a resistive thermometer is used to measure the change in resistance. A simple design is shown in Figure 3.
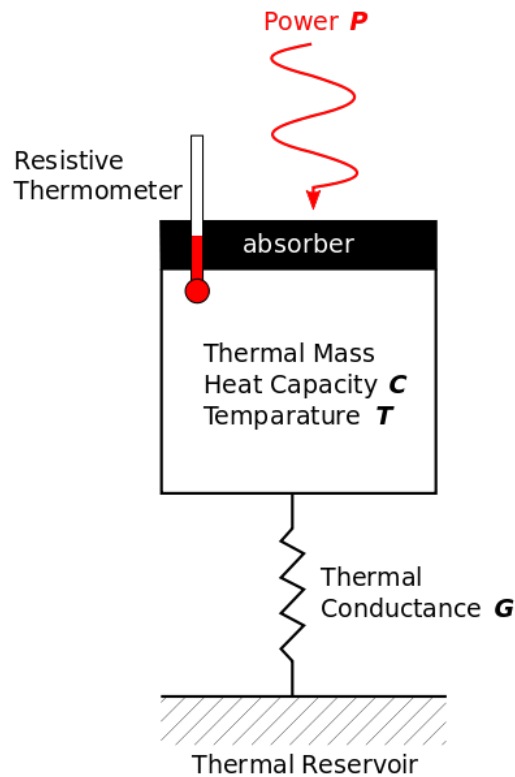
Figure 3.   Basic design of a bolometer. From [6]

The basic design is one where a silicon or germanium chip has been doped to give it a high thermal dependence on the electrical resistivity, as well as a resistance suitable for coupling the signal into an amplifier. These chips are generally coated with a

material to aid in the absorption of the electromagnetic radiation. The chips are then mounted between two electrical contacts by thin leads that supply the current path for the measurement, as well as the thermal link to dissipate the energy. Bolometers are slow to return to thermal equilibrium with the environment making them less suitable for applications requiring fast electromagnetic signals. The response time of the detector is an exponential with an electrical time constant (τ_E) of

$$\tau_E = \frac{C}{G - \alpha(T)P_1} \tag{2-1}$$

where C is the heat capacity of the material, $G = P_O/T_1$, P_O is the incident power, T_1 is the temperature difference above ambient, $\alpha(T)$ is the temperature coefficient of resistance and P_1 is the electrical power dissipated by the intrinsic resistance of the detector. These bolometer sensors can be combined into a grid to create a focal plane array that forms the basis for a bolometer camera. Due to the mechanism for which the electrical signal is linked directly to the resistivity of the material, bolometers lend themselves easily to use with superconducting materials.

b. Superconducting Bolometers

Superconducting bolometers utilize the superconducting nature of materials that are held near their critical temperature. At the critical temperature the rate of change of the resistivity with respect to temperature varies sharply (e.g., Figure 4).
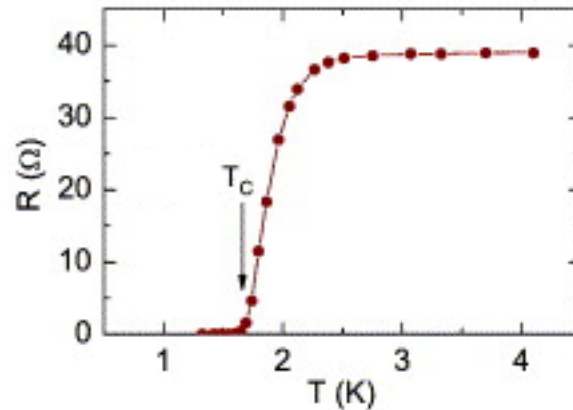
Figure 4.   Resistance of superconducting material near critical temperature (T_c). After [7]

If the bolometer can be stabilized in this region then the slight increase in temperature will cause a large increase in the resistivity resulting in a clear signal to be measured from a small amount of input radiation. Superconducting bolometers are regarded as the most sensitive of thermal detectors and have many applications by astronomers, astrophysicists as well as particle physicists.

B.   LOCK-IN MEASUREMENT TECHNIQUE

A lock-in amplifier (LIA) may be used to aid in the detection of small signals that may be well below the background noise of the detector. The LIA takes an input signal from the detector that has been modulated at a certain frequency as well as a reference signal from the modulation device and outputs a DC voltage that is proportional to the peak voltage of the original input from the detector.

The basic operation uses the orthogonality of sinusoidal functions to remove the frequency components of the unwanted noise. A diagram for the LIA process is shown in Figure 5.
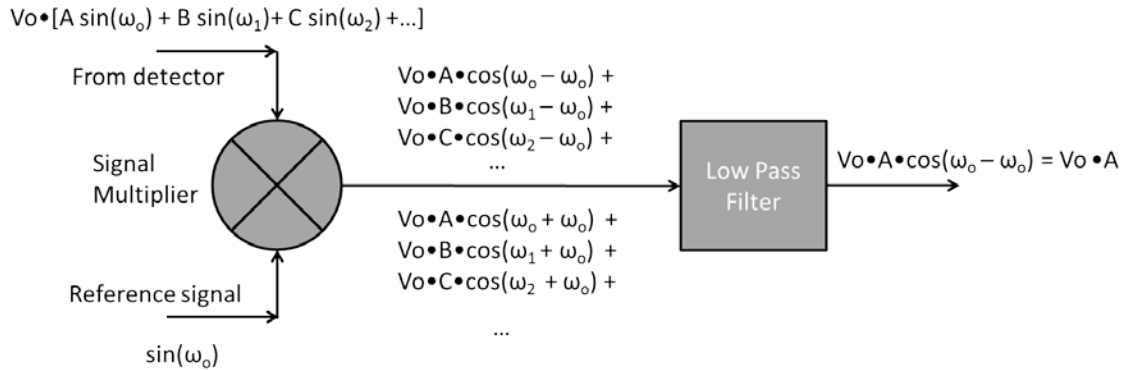
Figure 5.   Basic operation of lock-in amplifier

The LIA take two input signals, the output of the detector that includes noise components modulated at a reference frequency, $Vo \cdot [A \cos(\omega_o) + B \cos(\omega_1) + C \cos(\omega_2) + ...]$, and reference signal of the frequency the detector signal is being modulated at, $\sin(\omega_o)$, as shown in Figure 5. A noisy signal from the detector will have a large bandwidth but it will necessarily have a Fourier component at the modulation frequency

9

that was applied to it. The reference signal will have only the fundamental frequency that is modulating the signal. These two signal are multiplied and generate a new signal where the sum and difference frequencies are generated (ω_o - ω_o , $\omega_1 - \omega_o$, $\omega_o + \omega_o$, …). A low pass filter is then applied to the signal to cut out the higher-order frequencies leaving just the direct current signal ($V_o A$). From this, a direct current (DC) signal of the same amplitude as the incident signal can be extracted from the noise. [8] In optical measurements the signal to the detector is often modulated.

For many optical detection applications an optical chopper is used to modulate the light in a square wave pattern. An optical chopper consists of a chopper head, which has a DC motor and a chopper wheel, and a control box, which controls the angular velocity of the wheel and outputs the reference frequency. The chopper wheel is a disk with evenly spaced apertures (e.g., Figure 6); its angular frequency is controlled by the DC motor.

DIAMETER 4"

APERTURE .84"
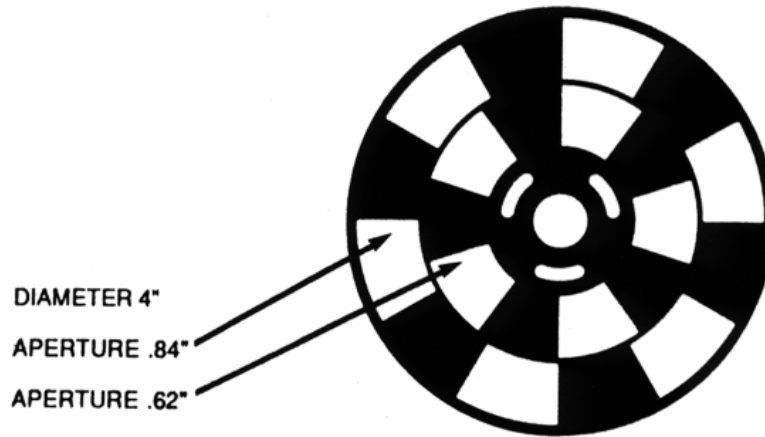
APERTURE .62"

Figure 6.   Chopper wheel. From [9]

Chopper wheels often have different sets of apertures at different radial positions that correspond to different chopping frequencies. The user selects a given set by the appropriate placement of the wheel with respect to the detector. A simple setup is depicted in Figure 7.
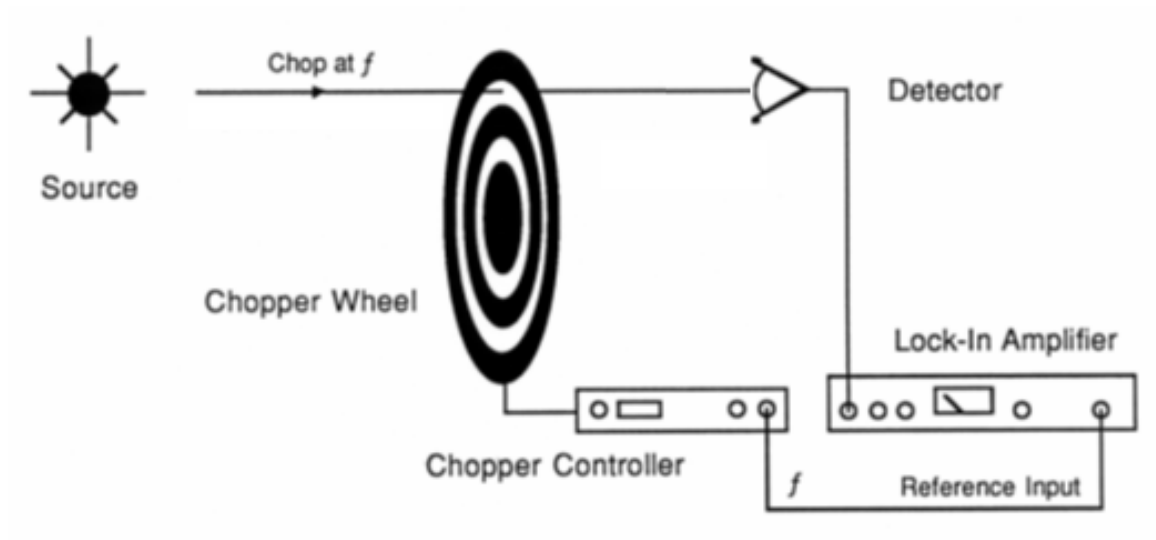
Figure 7.   Optical chopper and lock-in amplifier experiment. From [8]

The light source being measured propagates through the desired aperture of the rotating chopper wheel. This imparts square wave modulation to the signal that is then measured by the detector. This modulated signal from the detector is then sent to the input of the lock-in amplifier. The reference frequency of the modulation from the chopper control box is attached to the reference input on the lock-in amplifier. This allows the lock-in amplifier to output a DC voltage that is proportional to the detector output. Care must be taken in deciding modulation frequency as the period of modulation must be longer than the detector's response time, and the frequency also must stay inside the bandwidth of the lock-in amplifier. This technique allows for small signals to be measured that are well below the noise threshold of the detector, often permitting several orders of magnitude decrease in the minimum detectable signal. In a detector with a noise background of 1 mV a signal as small as 10 μV can be measured with ease.

THIS PAGE INTENTIONALLY LEFT BLANK

III.   IMAGING TRANSPORT SYSTEM

The relativistic electrons that are used to generate the THz radiation can have an unwanted effect in the creation of ionizing radiation that is a danger to users and equipment. As a result FEL's are placed inside large vaults, or concrete enclosures, to protect the researchers in the surrounding area from potentially harmful radiation. It also means that sensitive electronic devices inside the vault may need to be protected from damage. For this reason, it is desirable to have the diagnostic station for the FEL outside of the vault in a place where the equipment and scientists can safely operate. This leads to a long transport path of the THz radiation from the FEL to the diagnostics. The combination of the vault geometry, the long transport path, and the long radiation wavelength leads to several design issues when planning the transport path and optics.

A.   ALIGNMENT

The long transport path and small detector size causes alignment to be very important. To aid in this alignment, a visible laser will be used to align the optics of the system. It is desirable for the optic elements of the transport path to direct the THz radiation in the same manner as visible radiation. There are certain lens materials that have the same refractive index at THz and visible frequencies, but they are relatively expensive and generally do not come in large sizes [10]. To meet the alignment requirements of the Niowave system, metallic mirrors are the best option for the transport system. Mirrors can be made into off-axis parabolic shapes to supply focusing to a beam in a similar manner as a spherical lens while also supplying directional control, minimizing the number of optics needed.

B.   DIFFRACTION

The radiation produced by the electron beam will have an initial transverse electric field distribution that is the same as the electrons' spatial transverse distribution, which ideally has a Gaussian profile. The THz radiation will undergo diffraction, and due to the Gaussian mode, it will expand following Eq. (3-1)

$$w(z) = w_o\sqrt{1 + \left(\frac{z}{z_r}\right)^2},$$ (3-1)

where w_o is the mode waist radius, z is the propagation distance from the waist, and $w(z)$ is the optical radius at position z. The Raleigh range (z_r) is defined as the distance the beam must propagate from the waist before the radius increases by $\sqrt{2}$ (or, equivalently, the area doubles). In terms of the optical waist radius, w_o, and the wavelength, λ, the Raleigh range is

$$z_r = \frac{\pi w_o^2}{\lambda}.$$ (3-2)

The THz radiation is created by the electron bunches so that the optical waist radius is approximately equal to the electron beam radius. The small electron beam of ~3mm radius and the long wavelength of radiation, 150 µm–300 µm, cause the wavefronts to expand quickly. This must be taken into consideration when designing the layout and size of optics being used for transport.

A true transverse Gaussian profile has infinite tails that are truncated when reflected by a real mirror of finite radius. The fractional power loss, F, for a transverse Gaussian beam being reflected by an optic with a circular aperture is

$$F = 1 - e^{-a^2/w^2(z)}.$$ (3-3)

where a is the optic radius. To mitigate the power loss through the transport system the beam should be kept small in comparison to the optics and the number of optics should be minimized.

C.   VAULT GEOMETRY

The FEL vault has approximately two meter thick concrete walls as well as a 2 meter thick ceiling. There are conduit pipes through this shielding to the roof of the vault that are large enough for an optical transport system while maintaining the necessary shielding. This scheme allows the most accessible location for an optical diagnostic station. A diagram of the geometry inside the vault is shown in Figure 8.
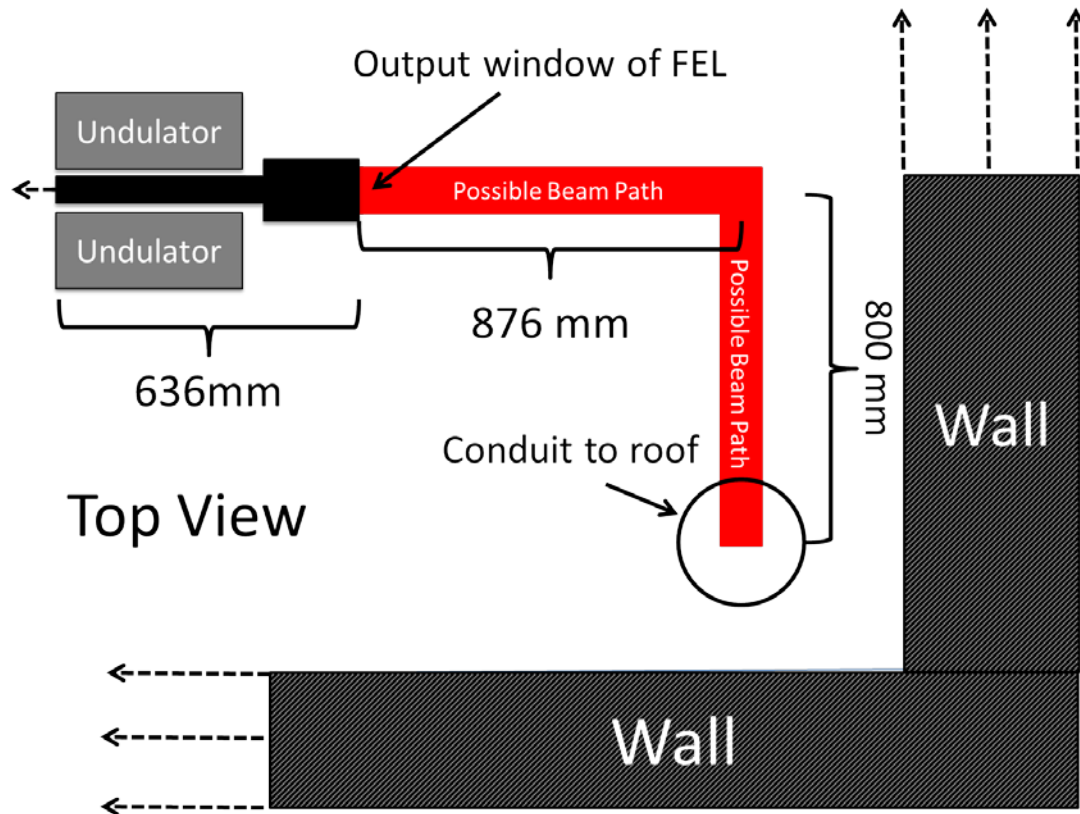
Figure 8.   Diagram of vault as viewed from above with the FEL and
vertical conduit to roof

Inside the FEL, the electron beam transits through a thin 25.4 mm diameter beam pipe while interacting with the magnetic fields in the undulator to create the radiation. After the undulator, the beam pipe expands to 34.8 mm diameter and in this portion of the beam pipe a dipole magnet (not shown) directs the electron beam to a beam dump below the beam line while leaving the THz radiation to propagate. The THz radiation then exits the beam line through a 22 mm diameter crystal quartz window. The center of the 305 mm diameter conduit that will be used to transport the radiation is 876 mm past the FEL window and 800 mm to the side. The radiation must be collimated and transported to the conduit where another mirror will direct the beam to vertical. The transport geometry out of the vault is shown in Figure 9.
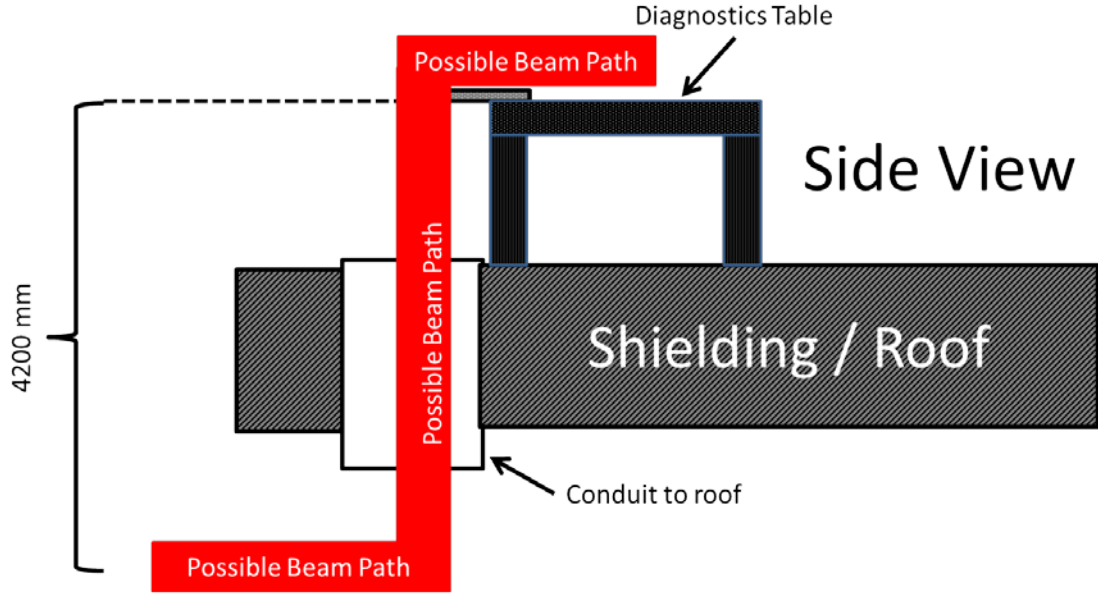
Figure 9.   Geometry of transport to diagnostic station viewed from the side

The height from the beam line to the diagnostic station is ~4200 mm. The beam must be directed through the conduit while remaining smaller than the optical elements at the diagnostic station that will focus the light and direct it to the measurement devices.

The overall design philosophy will be to use a freely propagating path that (1) first collimates the light at a close distance from the output of the FEL to keep the radius a reasonable size, (2) transport the collimated light several meters to the diagnostic stage, (3) then refocuses the light onto the detector or spectrometer. This setup will require two or three focusing optics (in the form of off-axis parabolic mirrors) depending on the setup chosen.

D.   BEAM TRANSPORT SIMULATION

A simulation was written that follows the complex curvature of the Gaussian laser beam as it traverses an optical transport system. The complex curvature of the Gaussian beam, q, contains information on the size and wavefront curvature and is defined by

$$\frac{1}{q} = \frac{1}{R} + i\frac{\lambda}{\pi w^2} \tag{3-4}$$

where R is the radius of curvature of the beam, and w is the transverse size of the beam. In simulating the optical FEL output, the wavefronts are assumed flat at their creation

16

$(R \rightarrow \infty)$. The change in the complex curvature as it transits open space can be calculated by Eq. (3-5),

$$q(z) = q(0) + z,$$ (3-5)

where $q(0)$ is the initial complex curvature and z is the distance propagated [11]. The effect that a lens (or an off-axis parabolic mirror) has on the complex curvature is

$$q(z) = \left(\frac{1}{q(z)} - \frac{1}{f}\right)^{-1}$$ (3-6)

where f is the focal length of the optic. Throughout the propagation path the beam waist size can be calculated by Eq. (3-7),

$$w(z) = \sqrt{\frac{-\lambda}{\pi \, \text{Im}(\frac{1}{q(z)})}}.$$ (3-7)

The simulation tracks the beam radius and complex curvature as the beam traverses the optical path with distances of propagation and placement of optics decided by the geometry of the vault depicted in Figure 8 and Figure 9.

E.   FIRST OPTIC PLACEMENT

The electron beam emits light continuously as it transits the undulator. Both the extended nature of this radiation source in the undulator and the large diffraction of the optical wavefront must be considered when deciding the distance from the output window to the collimating optic. Radiation created along the entire length of the undulator must be collimated by the same initial optical elements and transported to the detector without excessive power loss. This places a limit on the distance to the first collimating optic from the undulator. If the collimating optic is placed too close to the output window of the FEL, then the radiation created at different parts of the undulator will not be equally well collimated, which can lead to power loss throughout the rest of the transport system from the leakage of radiation around optical elements.

Figure 10. Depicts the optical 150 µm optical beam profile as it transverses a transport system for close placement of collimating optic near the FEL output window (A), and placement of collimating optic ~ 1 m away (B)

This situation is depicted in Figure 10 showing the 1/e radius of the radiation electric field created at beginning (blue), middle (red), and end (green) of the 33 cm long undulator as it propagates through a transport system. The thick black lines at left depict the position of the surrounding beam pipe and the output window of the FEL. The thin black vertical lines depict the position and the radius of the focusing optics in the transport system. An initial beam waist of 3 mm generating 150 µm radiation was used in the simulation of each trace. In Figure 10A, the collimating optic is located 658 mm from the origin at the beginning of the undulator and puts it just outside the output window. The collimating optic's close position to the source causes the beam radius to be small when it is collimated, but does not collimate all parts of the beam equally. This unequal collimation results in more clipping at the focusing optic, which is located at a distance 5658 mm from the origin.

Figure 10B depicts the same setup but with the collimating optic moved back to 1588 mm. This larger distance allows the beam radius to grow before the beam is collimated for transport onto the final optic. For each position the focal length was optimized by scanning through a range of focal lengths and calculating the total clipping of the three profiles on the final optic. The same simulation was done with a 300 µm beam and is shown in Figure 11.
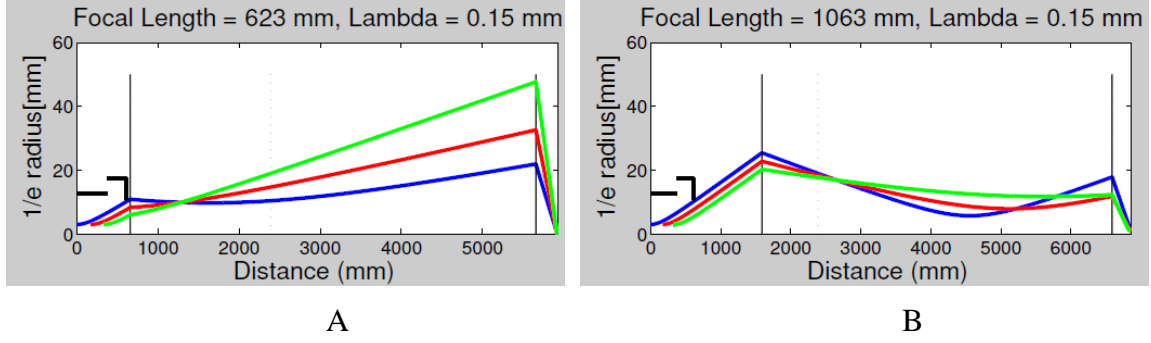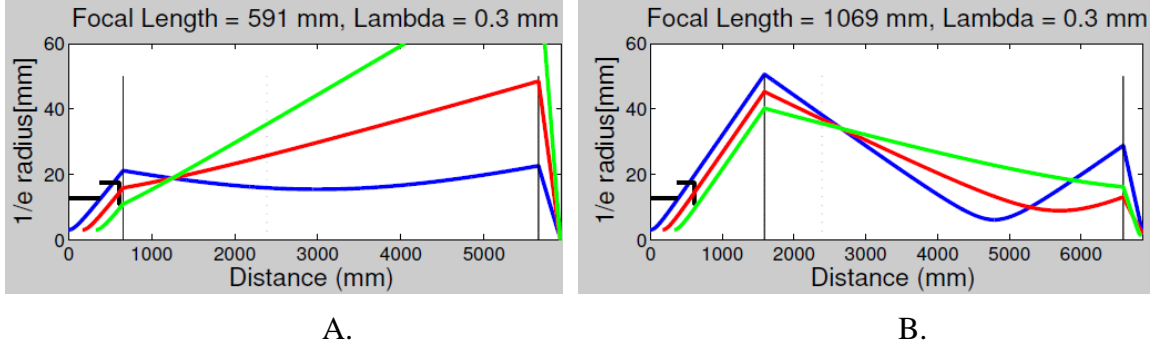
Figure 11. Depicts the optical 300 µm optical beam profile as it transverses a transport
system for close placement of collimating optic near the FEL output window
(A), and placement of collimating optic ~ 1 m away (B)

Figure 11 shows the same simulation but at a longer wavelength of 300 µm. Both the close collimating optic (Figure 11A) and the far collimating optic (Figure 11B) show the same trend as the 150 µm example, but now more of the beam is clipped inside the beam pipe and the output window. The simulation does not perform the actual clipping, but it is evident from the diagrams. The simulation takes into account clipping by the beam pipe and window when calculating the total power lost. The larger beam radius on the collimating optic allows the radiation created at different portions of the undulator to be similarly focused so the radiation is well within the radius of the next optic. More power is lost on the initial optic from the larger beam radius. These two consequences of the initial optic placement must be balanced to meet the goal of the transport system. For both the 300 µm and 150 µm cases, it was better to have the first optic at the 1588 mm location.

F.   FOCAL LENGTH SENSITIVITY

The large transport distance and the large size of the laser beam due to diffraction make it difficult to procure optics for the transport system. Optics up to 100 mm in diameter, which will help capture most of the radiation, with the focal lengths needed to meet the geometry of the transport path, are not easily procured. The lack of off the shelf mirrors and excessive costs for custom ordered optics impose the need to fabricate these mirrors at Niowave's machine shop. In recognition of the fact that a machine shop can only manufacture a focusing mirror to the desired focal length to within certain tolerance,

19

the transport design's sensitivity to the focal length should be minimized to decrease the tolerances that the machine shop needs to satisfy. Two separate transport designs were considered when studying the focal length sensitivity; one utilizes a single off-axis parabolic (OAP) mirror in the vault to collimate the radiation for transport to the roof; the second utilizes a pair of OAP mirrors in the vault to collimate and direct the radiation.

1.   Single OAP Transport System

A transport system utilizing a single OAP mirror to collimate the radiation for transport to the roof is depicted in Figure 12.
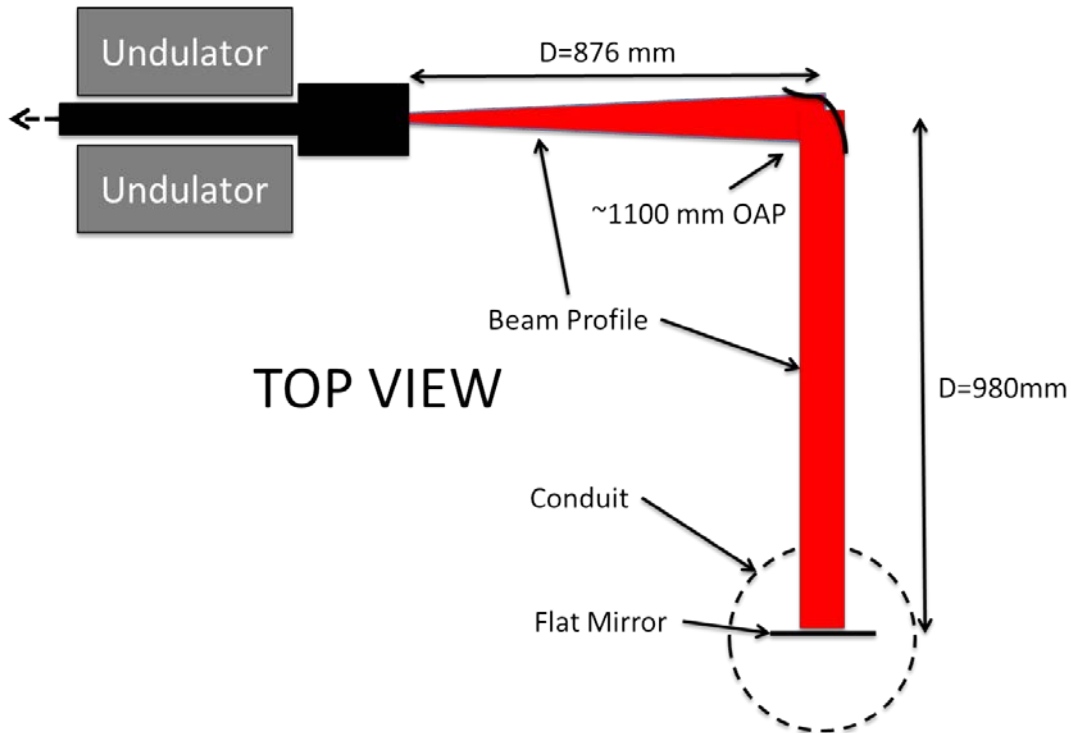
Figure 12.   Diagram of single OAP transport system

The THz radiation exits the window of the FEL and propagates freely until the first 90 degree OAP mirror that is ~870 mm away. In this case, there is not much freedom to place the collimated optic since it must be positioned in line with the conduit. This OAP mirror collimates and directs the radiation towards the conduit where a flat mirror is used to direct the radiation out of the vault. At each optic or aperture in the transport system

20

the power loss due to leakage or clipping was calculated using Eq. (3-3). The total power loss due to leakage was calculated for a range of focal lengths for the OAP.
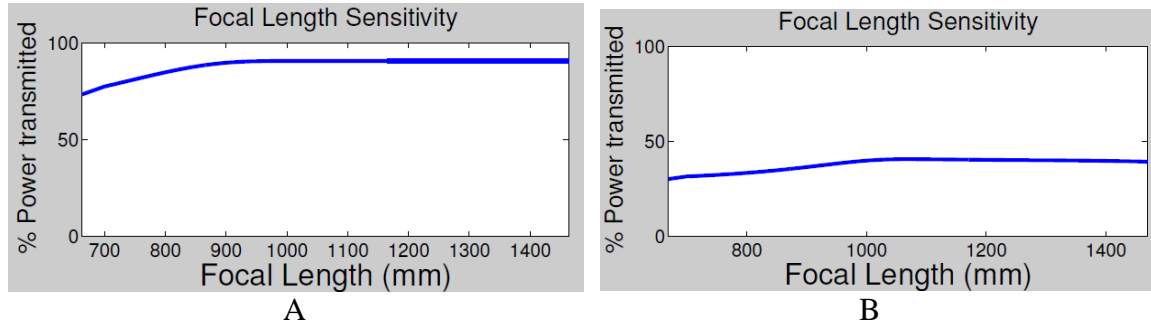
Figure 13.   Focal length sensitivity of single OAP transmission system for 150 µm (A) and 300 µm (B).

Figure 13A and 13B show the transmission percentage of the transport system for 150 µm and 300 µm radiation, respectively, for a range of focal lengths of the single OAP mirror. The 300 µm case has ~40 percent less transmission efficiency due to the large divergence of the optical beam resulting in more clipping at the output window of the FEL and the first optic. Focal lengths up to ±36 percent from the maximum were scanned and the transmitted power showed marginal dependence on the focal length.

2.   Dual OAP Transport System

Another possible optical transport setup involves a pair of OAP mirrors to act in tandem to collimate the radiation. The design is depicted in Figure 14. Again, the first optic must be placed in line with the vertical conduit. This dual OAP transport system allows some adaptability in the collimation strength of the lens system by adjusting the distance between the OAPs.
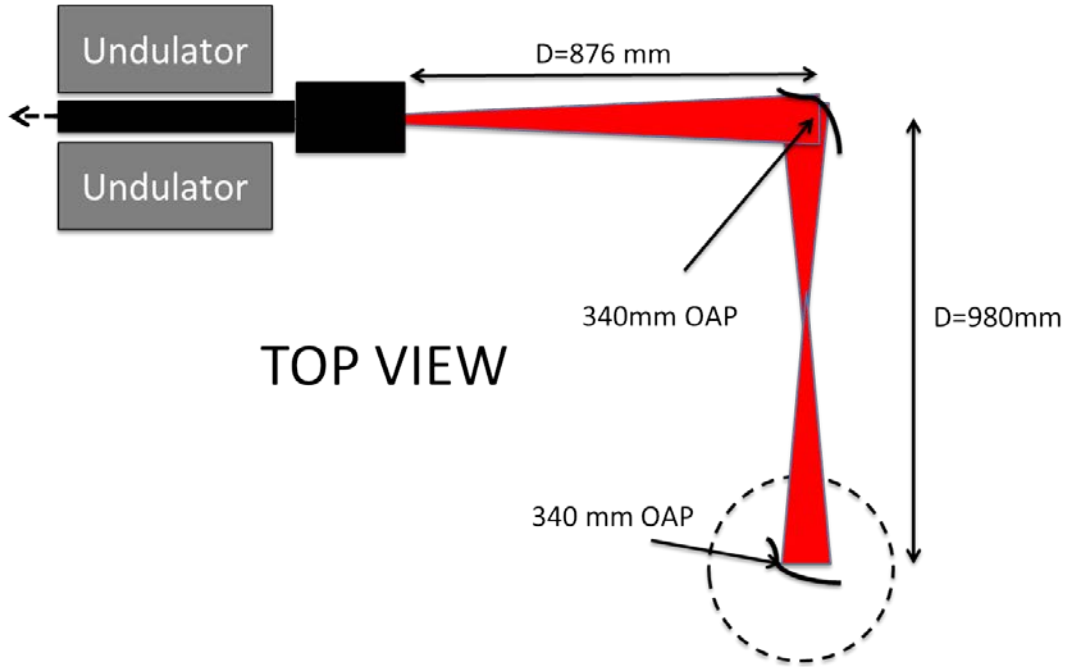
Figure 14.   Diagram of double OAP transport system

Figure 14 depicts a transport system where two OAP mirrors are used to collimate the THz radiation. The radiation is free to expand until the first OAP mirror where it is turned and focused. A second OAP located at the conduit then collimates the expanding beam and directs it vertically towards the diagnostic table. The same simulation was done as the single OAP case. The results are shown in Figure 15.
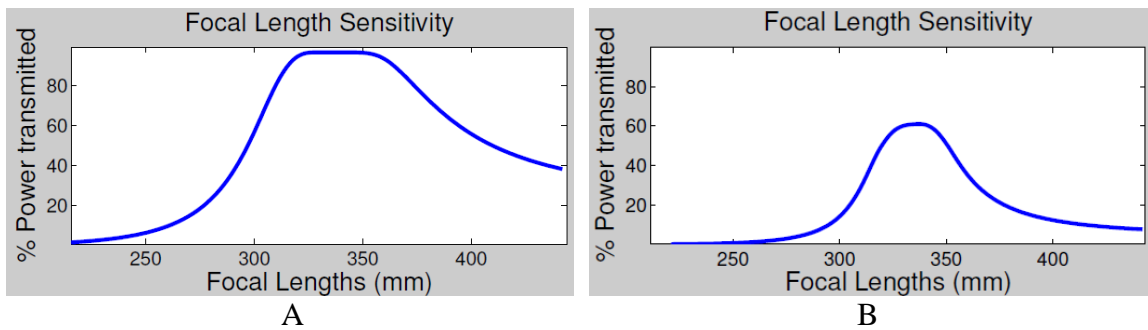
Figure 15.   Focal length sensitivity of dual OAP transmission system for 150 µm (A) and 300 µm (B)

For the dual OAP system simulation, the focal length was again varied by ±36 percent from the maximum transmission focal length of 340 mm. The two OAP focal lengths were kept equal and the distance between them was kept constant. This causes a sharp dependence on the focal length for the radiation to be properly collimated. However, for focal lengths away from the optimum, the distance between the optics could be adjusted to maintain proper collimation of the radiation, though the separation distance is subject to the design constraints of the geometry of the transmission system. With a conduit diameter of ~300 mm, there is room to adjust the sensitivity ± 150 mm. With this amount of flexibility, focal lengths of 290 mm to 390 mm can be accommodated with the current geometry.

G.   ELECTRON BEAM ALIGNMENT SENSITIVITY

While electron beams should ideally be collinear with the axis of the beam line, this is not always the case. The electron beam can have a transverse offset from the center of the beam pipe as well as a slight angle in its trajectory. If the electron beam is misaligned, it would cause light created at the different portions of the undulator to be directed differently by the optics. A ray-tracing simulation was written to study the effects of an extended non-collinear source [12]. The simulation follows a central ray, which follows the center of the Gaussian beam, as well as two extremal rays that define the envelope of the Gaussian beam. These extremal rays have an initial divergence angle from the center ray given by Eq. (3-9).

$$\theta \approx \frac{\lambda}{\pi w_o}.$$
(3-9)

This angle takes into account the wavelength, λ, and the beam waist, w_o, and can accurately describe the beam radius in the far-field region. The simulation follows the matrix method of calculating the beam ray position and angle as it propagates and is focused.

1.   Single OAP Transport System

Two simulations were performed: one where the angular and spatial offsets are zero, and the second representing the likely worst case operating scenario, where there is

23

a 2 mm spatial offset and a 6 mrad angular offset [12]. Both of these initial conditions are shown in Figure 16 where a single OAP was used to collimate the beam (see Figure 12).

Figure 16. Single OAP transport system electron beam alignment study for aligned electron beam (A) and misaligned electron beam (B)

The case demonstrated are for 150 µm wavelength radiation and an initial beam radius of 3 mm. If the electron beam is in the ideal case with no offsets, Figure 16A, then the radiation will remain centralized on the mirrors through the transport system and avoid excessive clipping by the beam pipe and output window. In the worst operating case scenario, Figure 16B, the radiation wanders off of the mirror centers and is clipped heavily by the beam pipe and the output window. The radiation is still transported to the final optic but the power will be diminished by roughly 50 percent and the focus will not be in the expected place. The central ray of each envelope denotes the direction of the wavefront of the radiation. This can be seen in Figure 16B as the angle of the central ray. Tilted wavefronts could lead to problems in spectroscopy measurements where interference methods are used [13].

In Figure 17 the single mirror OAP transport system was rerun with a 1300 mm focal length allowing a larger beam on the final mirror.
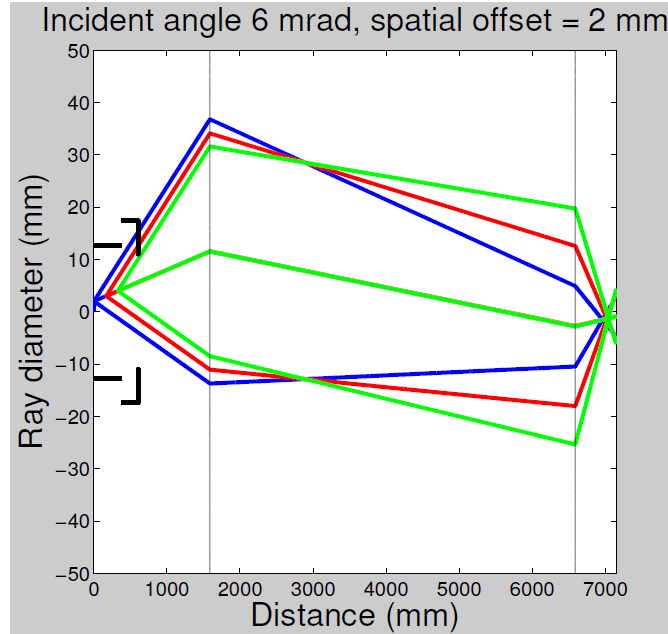
Figure 17.   Single OAP transport system electron beam alignment study, 1300 mm focal length

As seen in Figure 17 changing the focal length from 1100 mm to 1300 mm for the worst case scenario electron beam creates a more centralized optical beam with less convoluted wavefronts after the focusing optic. At the risk of losing power on the last optic due to a less focused beam, getting a better wavefront and a more predictable focus location could make up for this deficiency.

2.   Dual OAP Transport System

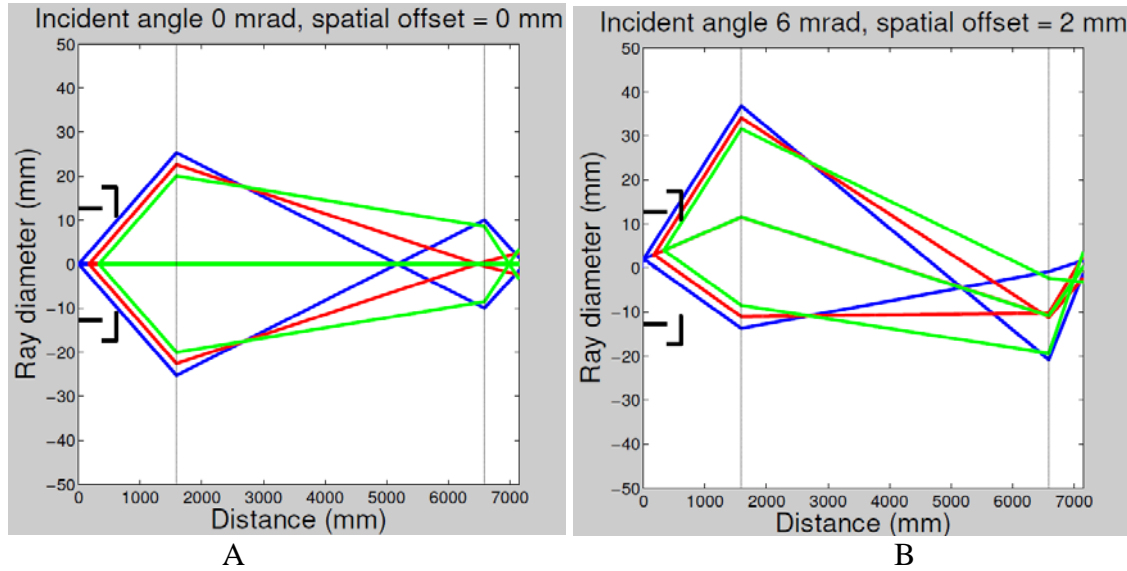The same simulation was done using the dual OAP focusing system (see Figure 14).
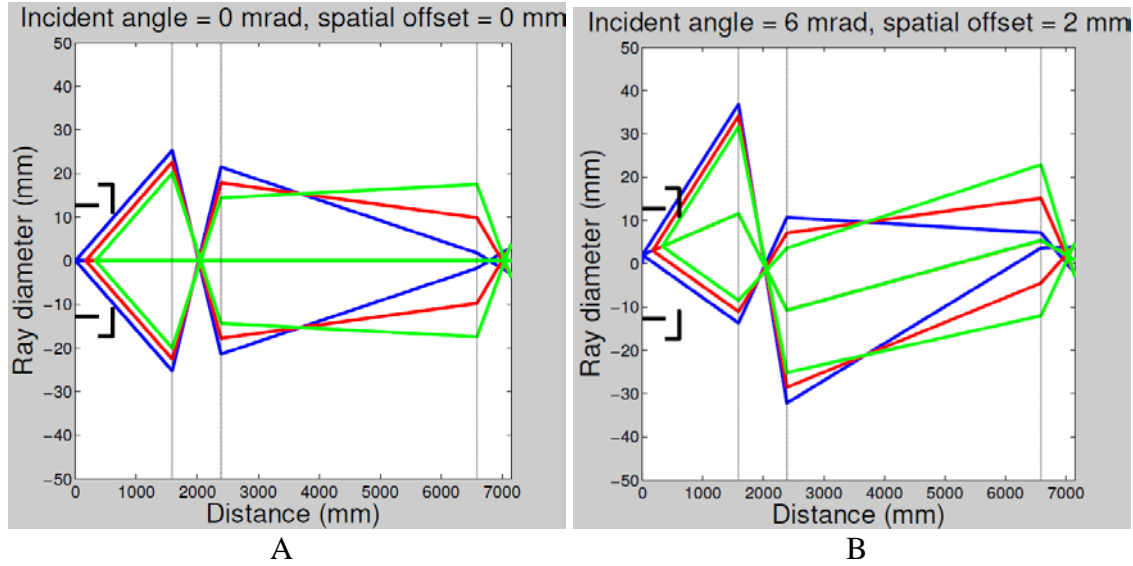
Figure 18.   Dual OAP transport system electron beam alignment study for aligned electron beam (A) and misaligned electron beam (B)

Just as the single OAP case in Figure 16A, the dual OAP transports the ideal case (Figure 18A) onto the center of the final optic. The worst case dual OAP (Figure 18B) has the same problems as the single OAP (Figure 16B) in the clipping at the undulator and output window but handles the rest of the transport system just as well as the example in Figure 17 and maintains the beam centroid on the optics.

IV.   NON-IMAGING TRANSPORT SYSTEM

The need for transporting the optical beam out of the vault can be avoided with planning and certain precautions regarding the diagnostic devices being used. During initial commissioning of the FEL the main diagnostic assessment that will be needed is a power measurement to allow the operators to optimize the accelerator and thus maximize the signal. For this reason it is advantageous to take possible misalignment of an optical path out of the situation. Given enough localized shielding from the high radiation sources, the detector could be placed in the vault near the FEL output window, greatly decreasing alignment and transport issues. This chapter discusses a robust non-imaging transport system that requires no optical alignment for placement of the detector inside of the vault.

A.   PHYSICS OF ELECTROMAGNETIC WAVE REFLECTIONS

When an electromagnetic (EM) wave is incident on a boundary there is reflection and transmission depending on the angle of incidence, the difference in material properties, and the frequency of the incident wave. Figure 19 shows an unpolarized EM wave reflecting off of a conducting boundary.
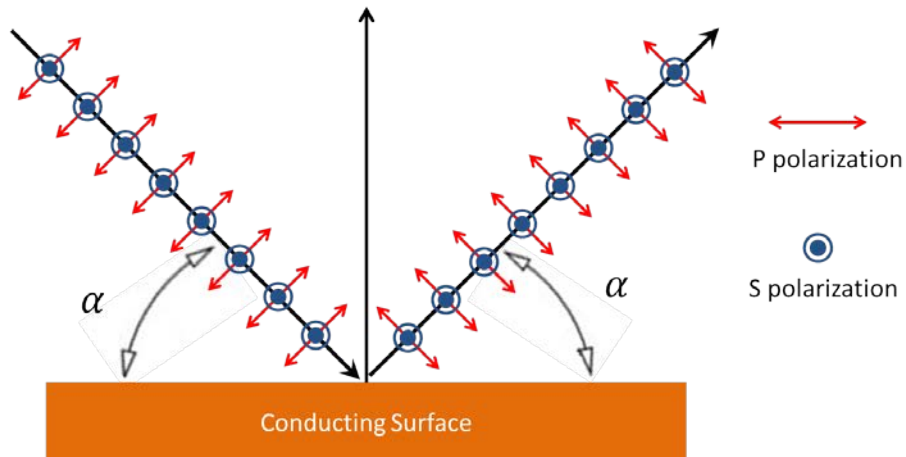

Figure 19.   EM wave reflecting off a conducting surface

The direction of travel is depicted by the black line and is incident at a grazing angle α. The radiation has both polarizations, or direction of electric field, and is depicted as the S and P polarizations. The P polarization is in the plane of incidence of the EM radiation while the S polarization is orthogonal to it (and therefore in the plane of the surface). The reflection coefficients for the S polarization, R_s , and P polarization, R_p, at grazing incidence (where the small angle approximation $\sin(\alpha) \approx \alpha$ can be used) is given by

$$R_s \approx 1 - 2x\alpha \qquad (4\text{-}1)$$

and

$$R_p \approx \frac{2\alpha^2 - 2x\alpha + x^2}{2\alpha^2 + 2x\alpha + x^2} . \qquad (4\text{-}2)$$

In Eqs. (4-1) and (4-2), α is the angle of incidence as depicted in Figure 19, $x = \sqrt{2\varepsilon_o \omega / \sigma}$, where ε_o is the permittivity of free space, σ is the conductivity of the material, and ω is the angular frequency of the EM wave [14]. The angle of incidence is equal to the angle of reflection and as the conductivity approaches infinity the reflection coefficients approach 1 (100 percent reflection).

Not shown in Figure 19 is the transmitted radiation into the conductor. The skin depth δ, where the electric field of the transmitted wave is depleted to 1/e of its original magnitude, is given by Eq. (4-3),

$$\delta = \sqrt{\frac{2}{\omega\mu\sigma}} , \qquad (4\text{-}3)$$

where μ is the permeability of the material, and σ is the conductivity of the material. For example, a 150 μm EM wave incident on a copper surface results in a skin depth of $\delta \approx 150$ μm, and for 300 μm radiation, $\delta \approx 214$ μm. This thickness must be taken into consideration when designing and procuring optics for use with longer wavelength radiation. If the conducting material of the optic is not thicker than δ, the optic will have reduced reflectivity for that wavelength. The use of highly reflective material can be used to create a transport path that requires no optical alignment with minimal loss (over reasonable distances).

B.   LIGHT PIPE

A light pipe is any sort of pipe (e.g., hexagonal or circular cross section) that uses reflections of EM waves at the inner boundary surface to contain and direct the radiation down a directed path. Light pipes can be used to channel radiation energy from one place to another in a simple, robust way. It is an economical and simplistic way to direct radiation when the phase information of the radiation does not need to be preserved. Due to the method of transporting, there are losses associated with using a light pipe that could be avoided using typical imaging optics. With each reflection, power is lost due to the finite conductivity of the metal as well as any impurities (oxidation) on the surface which may absorb the radiation. Also, since the metallic surface is not perfectly smooth, higher-order reflections could cause the radiation to require more reflections to make it to the end (or not make it at all). All of these effects can decrease the power transmitted through the light pipe. From [15] the theoretical transmission percentage can be derived from Eqs. (4-2) and (4-3), the light pipe properties, and the properties of the incident radiation. The result is given by Eq. (4-5),

$$T \approx \frac{1}{2}(1 + e^{-2q}) - \frac{q}{8F^2},$$
(4-5)

where $q = xL/d$ L is the light pipe length, d is the pipe diameter, $x = \sqrt{2\varepsilon_o \omega/\sigma}$, and $F = 1/2\alpha$ is the f-number of the incident radiation. Experimental results for several light pipes as well as theoretical curves based on Eq. (4-5) are shown in Figure 20.
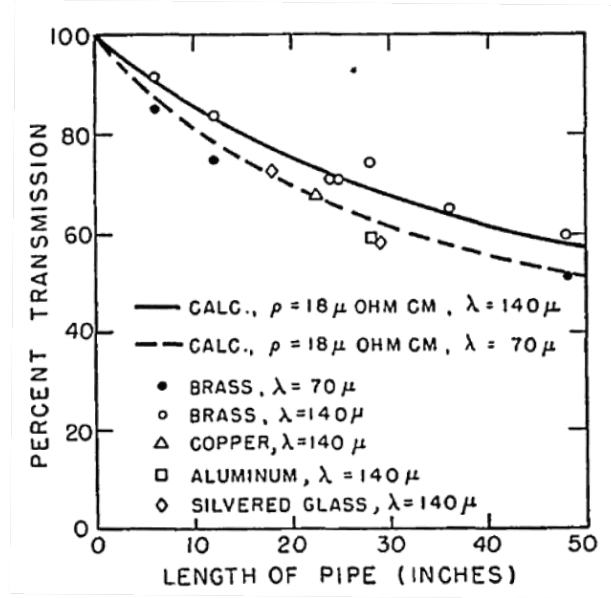
Figure 20.   Measured transmission in brass, copper, aluminum and silvered glass light pipes. From [15]

The experiment conducted by R.C. Ohlmann [15] measured the percent transmission through various light pipes (brass, copper, aluminum, silvered glass) of 1.1 cm diameter at 70 µm and 140 µm wavelength. These points are listed in the legend of Figure 20. The solid and dotted lines depict the theoretical curves generated from Eq. (4-5). While the theory matches the trend of the experimental results it is important to notice that the theoretical curves match closely with a resistivity $\rho=18$ µΩ-cm which is ~10 times larger than the value for copper and silver, and approximately seven times larger than that of aluminum. The reason for the shortcomings from the theory could be the higher order losses, the bandwidth of the radiation being used (shorter wavelengths will be attenuated more) as well as the disregard for skew rays in the derivation. While the theory shows some shortcomings, it is useful in showing ways to improve the device (e.g., larger diameter leads to better transmission). The experimental data shows that light pipes are a reasonable tool for transporting far infrared radiation over relatively short distances.

C.   CONE CONCENTRATOR

As mentioned before an obvious trend for light pipes is that a larger diameter leads to better transmission. While this is not a problem during transport, it is a problem when that radiation gets to a detector whose size will likely be much smaller than the diameter of the light pipe. Since the radiation is incident from anywhere in the light pipe with different angles and thus is no longer spatially coherent, conventional imaging optics cannot be used. To focus radiation without the use of imaging optics a cone concentrator can be used to channel the radiation. A light pipe can be made that tapers from a larger radius to the smaller radius of the size that is needed for the detector. While the cone concentrates the radiation, it is not perfect and may reflect some rays backwards. This is dependent on the magnitude of the tapering (how short the cone is for a given entrance aperture and exit aperture size), which cannot be too large or the radiation will be more likely to reflect backwards out of the cone.
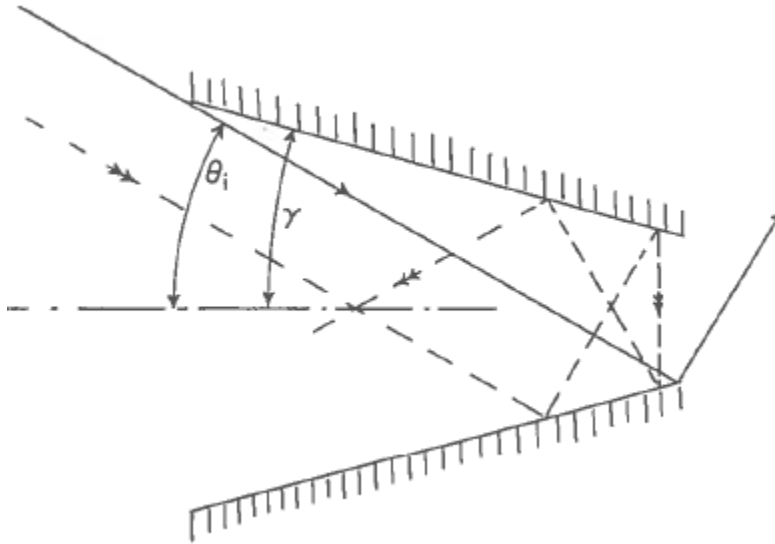

Figure 21.   Cone concentrator. From [16]

In Figure 21, a typical cone concentrator is shown. Two rays are shown with equal incident angle but with a spatial offset. The solid line ray simply reflects once and transits through the cone to the exit aperture. The dashed line ray has several reflections before being directed backwards. This demonstrates the non-ideal nature of the cone

31

concentrator and also demonstrates how some rays that are outside the desired radius will be directed through a smaller aperture. While some radiation does not make it through, there is a net increase in the intensity, so concentrators are commonly placed on the front of thermal detectors.

D.   SUMMARY OF NIOWAVE NON-IMAGING OPTICS SETUP

A simple non-imaging optical path was devised for the Niowave FEL that would allow for placement of the detector inside the vault. This helps make alignment over a long distance no longer necessary, though it limits the diagnostic information to the optical power (i.e., spectral information will then not be available in this configuration at the anticipated output power level). The system utilizes a one inch inner diameter copper pipe to trap and channel the radiation from the output of the FEL to the detector. A design constraint of the transport path was that the detector needs to be placed inside a shielded area with no direct line-of-sight between the electron beam path and the detector. This is to provide protection from the harmful high energy radiation created by the relativistic electron beam. This involves the detector being placed to the side of the beam line with steel blocks placed between it and the electron beam line. A depiction of the layout is shown in Figure 22.
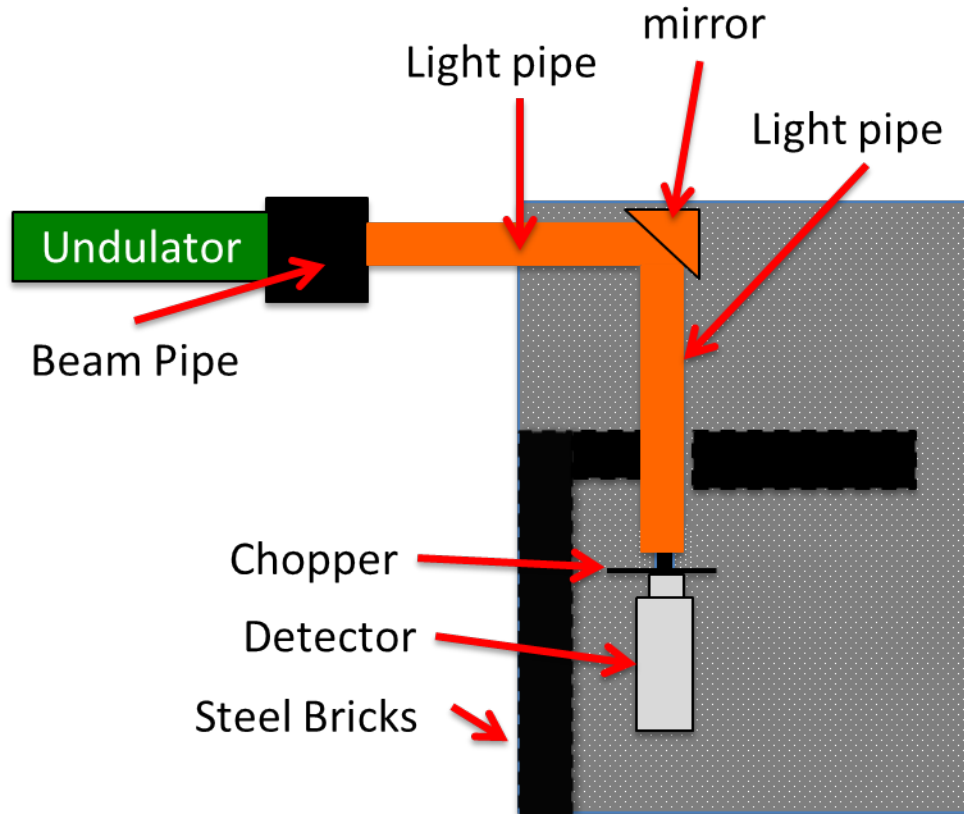
Top View

Figure 22.   Diagram of transport system with light pipe

The entrance of the light pipe was placed close to the 0.9 inch diameter output window of the FEL, so nearly all radiation that exits the FEL window enters the entrance aperture of the transport system. Halfway through the light pipe, a 90 degree bend was cut into the light pipe to allow the placement of a polished copper mirror to direct the radiation down the second leg of the light pipe. The exit aperture of the light pipe is at a diagnostic table where the detector and chopper head is placed. As was discussed in Chapter II, a chopper head is placed to modulate the radiation for easier detection with the use of a lock-in amplifier. The head of the detector is placed as close as possible to the exit aperture of the light pipe while allowing room for the chopper head to rotate. Shielding is stacked around the light pipe to protect the detector from high radiation

areas. The detector head itself has a cone that will concentrate the radiation from the 2.54 cm diameter of the light pipe to the 0.8 cm aperture of the detector. A picture of the final setup is shown in Figure 23.
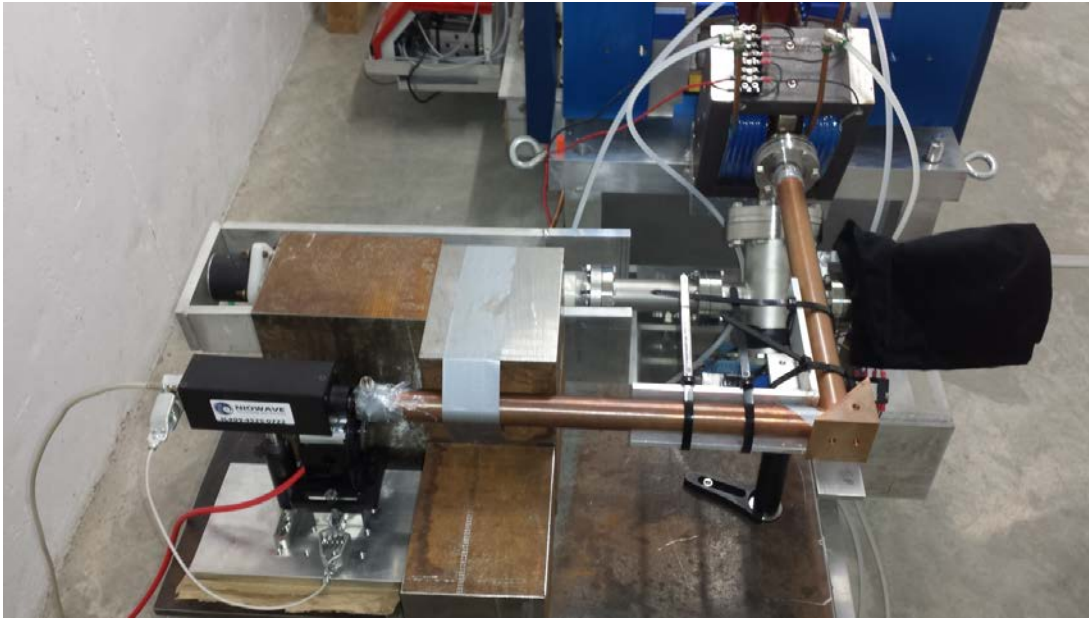

Figure 23. Picture of light pipe transport system in place at Niowave Inc.

The light pipe system allows for power measurements to be made with no chance of alignment errors. The light pipe also allows for an enclosed area that can be purged with dry nitrogen since water vapor is known to have large absorption bands in the THz regime [17]. The detector is surrounded by over four inches of steel on all sides that face the electron beam line and the electron beam dump. The detector output cable and the chopper control cable run out of the vault to a control room where they can be safely operated and monitored by personnel.

V. DETECTOR SYSTEM EXPERIMENTAL MEASUREMENTS

Before shipping the detector system to Niowave, the components were tested separately using a THz source at the Naval Postgraduate School (NPS) to prove they work as expected in the THz regime and to characterize the limits of the detector setup.

A. FEL OUTPUT WINDOW TRANSMISSION

The output window for the FEL allows for the radiation to be transmitted and utilized while maintaining the vacuum that is needed for FEL operation. It is important that the window material transmits the radiation at the designed wavelength of the FEL. An ultra-violet grade fused silica (UVFS) window was initially purchased and tested for its transmittance spectrum. To test this, a Fourier transform infrared (FTIR) spectrometer was used. The device utilizes a calibrated blackbody source and a Michelson interferometer to measure the spectrum [18]. The FTIR used has a mid-infrared range to measure between 2 μm and 25 μm and a THz range that measures from 30 μm up to approximately 120 μm. The transmission spectrum of the UVFS window was measured and is shown in Figure 24.
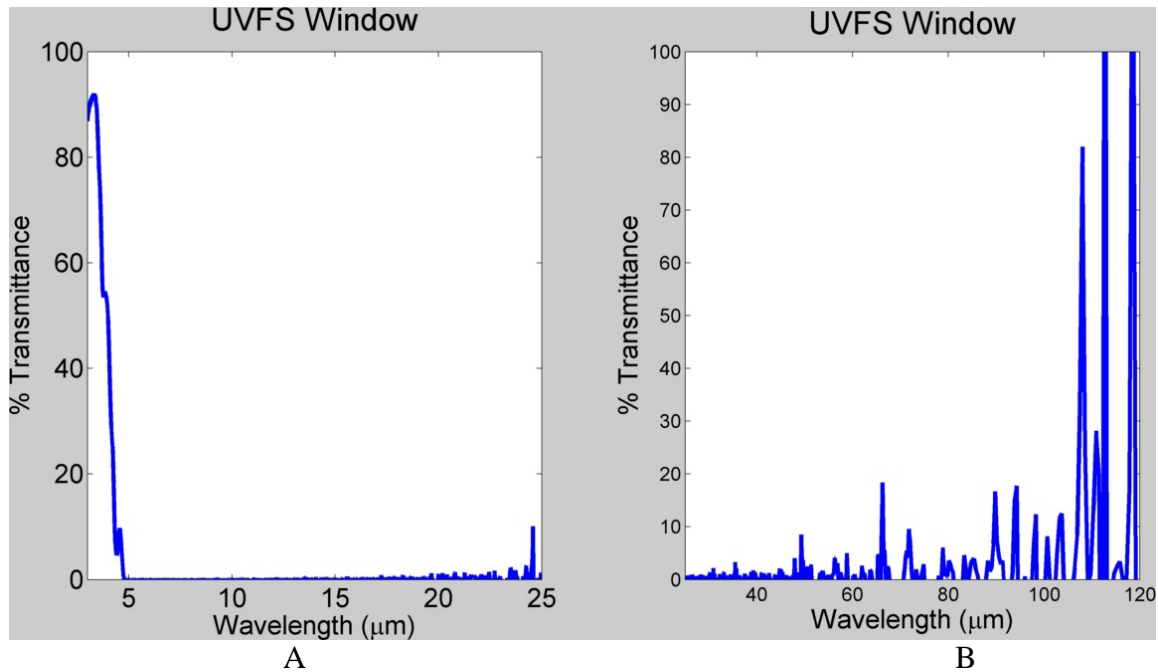
Figure 24. Transmission spectrum of UVFS window

In Figures 24A 24B, the transmittance of the UVFS is plotted as a function of wavelength. It can be seen in Figure 24A that the UVFS transmits well from the visible region through 3.3 μm before steeply dropping off to zero transmission. Figure 24B shows the transmittance for the 30 μm to 120 μm (THz) region. The small signal of the FTIR starts to be overcome by noise around 100 μm so the large peaks seen in Figure 24B may not represent actual spectral features. Figure 24 shows that UVFS is a poor transmitter for wavelengths between 3 and 100 μm. While the wavelengths the FEL will produce (150 μm to 300 μm) are outside the regime that the FTIR can measure (~1 μm to 100 μm), the spectrum shows a worrisome trend for the output window that requires more investigation. The results match with published results which state that it will be opaque at the FEL wavelengths [20].

To guarantee that the output window will not block the FEL radiation a fused quartz window was procured and tested in the same manner as the UVFS window. The results are shown in Figure 25.
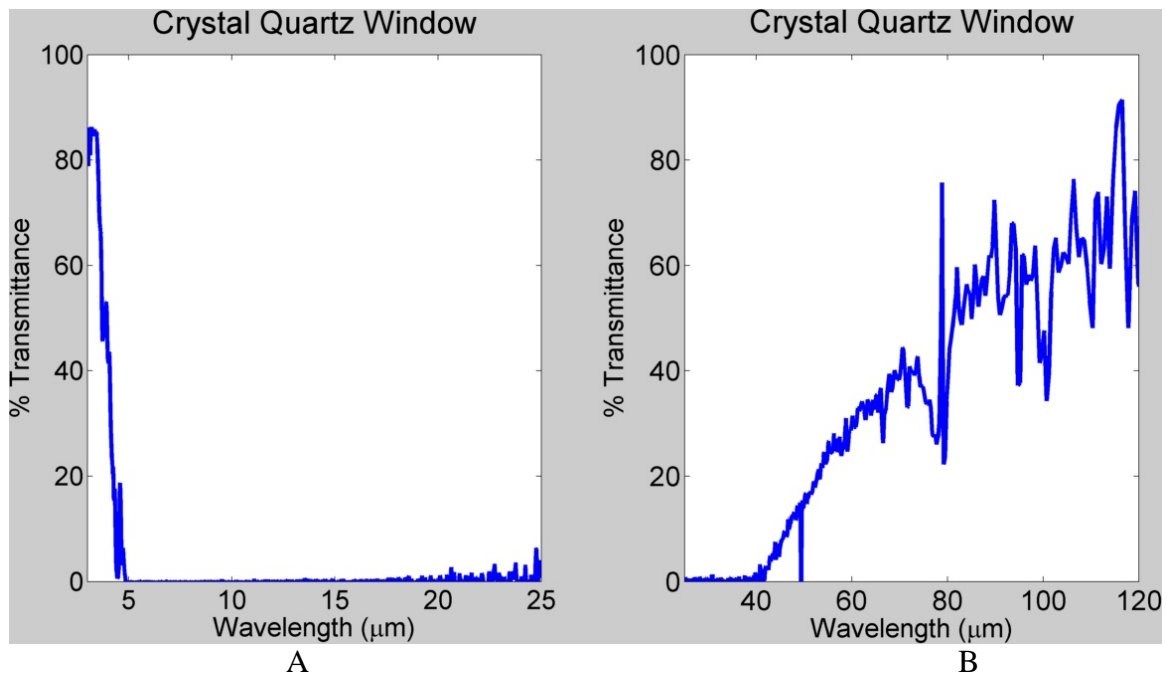
Figure 25. Transmittance spectrum for crystal quartz window

Like UVFS it has a peak transmission from visible through ~3 μm before dropping off. The key difference between the two materials is the increase in transmittance around 40 μm as seen in Figure 25B. While measurements above 100 μm tend to be noisy there is an obvious upwards trend in transmittance of crystal quartz above 40 μm. This measurement was compared with published literature values of the complex refractive index of crystalline quartz and the results are shown in Figure 26 [20].
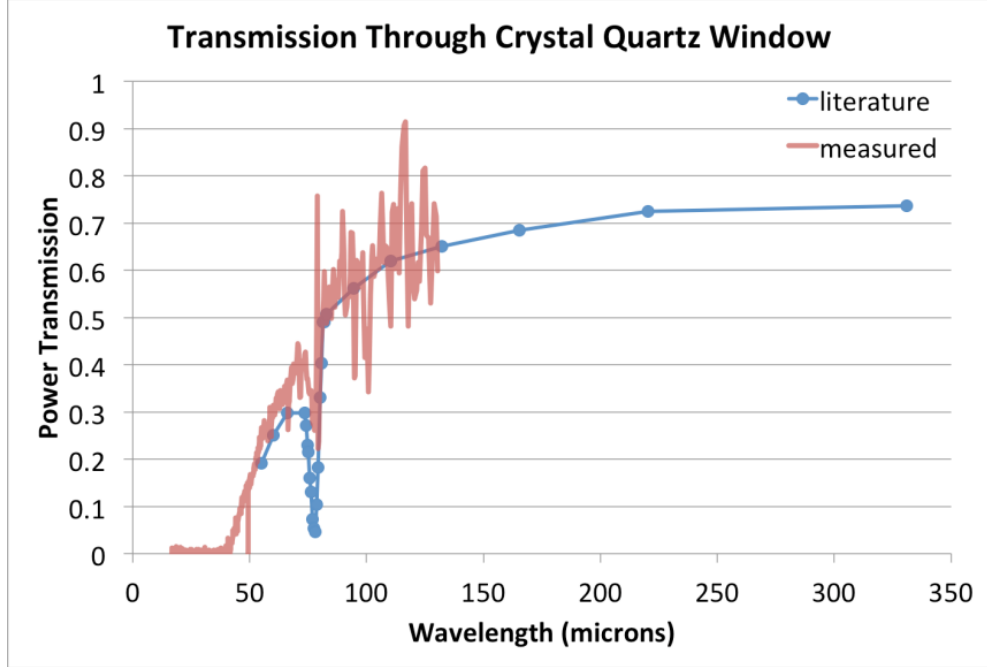
Figure 26.   Transmittance of crystal quartz compared with literature

Figure 26 shows the transmission spectrum for crystal quartz from 30 through 350 μm. The red line is the measured spectrum from the FTIR that was first shown in Figure 25B, the blue dots are calculated from measured values of the imaginary refractive index [18].   While the measured results from the FTIR have large amounts of noise, the agreement with the literature leads to a reasonable conclusion that the window has properties close to the sample in the literature and will transmit between 65 and 75 percent of the radiation in the desired wavelength range.   Therefore, crystalline quartz will be used as the window material for the Niowave THz FEL.

B.   MESH MIRRORS

Partially reflective mirrors are needed in many laser applications (e.g., Fabry-Pérot interferometer, laser cavity outcoupling), which is often accomplished for the THz regime by using a fine wire mesh. A detailed discussion of the theory regarding metal mesh mirrors can be found in [20]. A diagram of a generic mesh with the parameterizing dimensions labeled is shown in Figure 27.
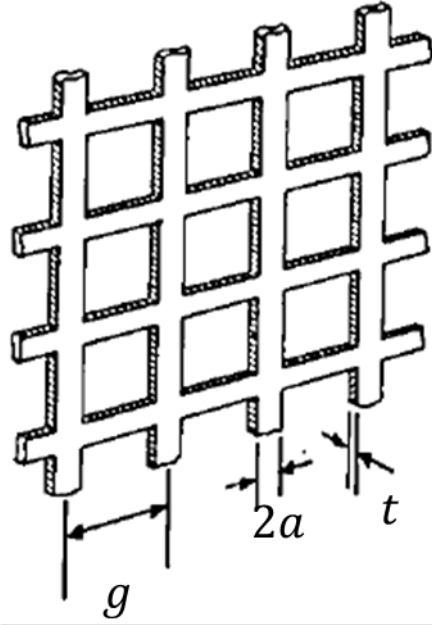
Figure 27. Diagram of mesh mirror. From [19]

The geometric parameters which define the reflectivity of the mesh include the mesh period, g, the grid spacing, a, and the thickness of the mesh, t as seen in Figure 27. It also depends on the conductivity of the material as well as the wavelength that is being reflected. The normalized loss resistance of the mesh is roughly estimated by

$$R_o = \left(\frac{g}{4a}\right)\sqrt{\frac{c}{\lambda\sigma}}, \tag{5-1}$$

where c is the speed of light, λ is the wavelength of radiation, σ is the conductivity, and g and a are the dimensions as shown in Figure 27 [20]. The admittance, Y, of the circuit (treated as a transmission line) is given by

$$Y = \frac{2}{R_o - iZ_o\left(\frac{g}{\lambda}-\frac{\lambda}{g}\right)^{-1}}, \tag{5-2}$$

where

$$Z_o = 2\ln\operatorname{cosec}(\pi a/g) \tag{5-3}$$

is the impedance. The impedance is the opposition to current, which in this case is caused by the oscillating electromagnetic field that interacts with the mesh. From this the complex amplitude reflection coefficient can be given by

$$\Gamma = -\frac{Y/2}{1+Y/2}. \tag{5-4}$$

39

The power reflection coefficient [21] is given by $R=|\Gamma|^2$. A copper wire mesh was procured for the Niowave THz FEL and its properties were measured. An optical measurement was taken of the mesh spacing using an Olympus BX51 system microscope and is shown in Figure 28.
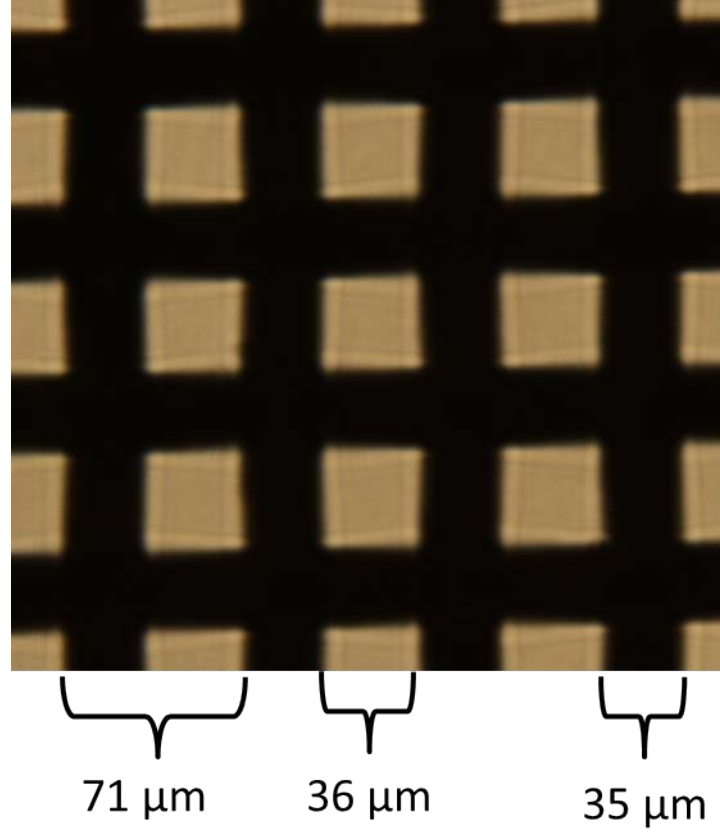

Figure 28.   Magnified image of mesh with measurements

In this mesh, $g = 71$ μm and $a = 35$ μm.   Substituting these values into the aforementioned theoretical equations leads to Figure 29.
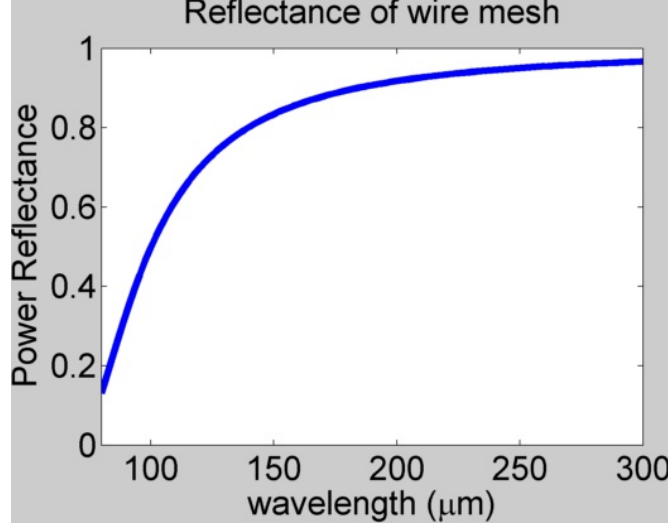
Figure 29. Theoretical reflectance of wire mesh.

Figure 29 shows $|\Gamma|^2$ as function of wavelength. It demonstrates an increasing reflectance at longer wavelengths. In the 150 μm to 300 μm wavelength range at which the Niowave THz FEL will be operating, the wire mesh will theoretically provide between 80 and 96 percent reflectance. Differences from the theory can come about from the fabrication of the metal mesh. Since the mesh under considerations is a woven metal cloth, the electrical contact between strands is not known and may be less than ideal which would degrade the reflectance. Also, the theory ignores the thickness of the grid (i.e., it assumes $t<<2a$) which could lead to disagreement.

C.   DETECTOR MEASUREMENTS

A pyroelectric detector was chosen for the Niowave FEL as it supplies the necessary sensitivity while also being simple to use and robust. The chosen detector was purchased from Microtech Instruments, Inc. and has a typical responsivity of 1000 V/W and a typical noise level of 1.0 mV. It has a spectral bandwidth from 100 μm to 15 mm [22]. Due to the choice of pyroelectric detector an optical chopper is needed to modulate the power and allow the measurement of heat flow.

To test the detector an existing quantum cascade laser (QCL) at NPS was used as the THz source. It was the best choice available to test the detector due to (1) it produces 80 μm radiation which is close to the desired wavelengths that will be measured from the

FEL, (2) it is easily gated as a square wave to simulate what an optical chopper will do to the radiation, and (3) it allows precise control over the relative output power so minimum power levels can be measured. The detector was placed at the focus of a polyethelene lens focusing the THz radiation onto the active area of the detector. To characterize the detector, a large signal was generated using the QCL with its internal gating (i.e., not using the separate optical chopper). The oscilloscope trace of the result is shown in Figure 30.
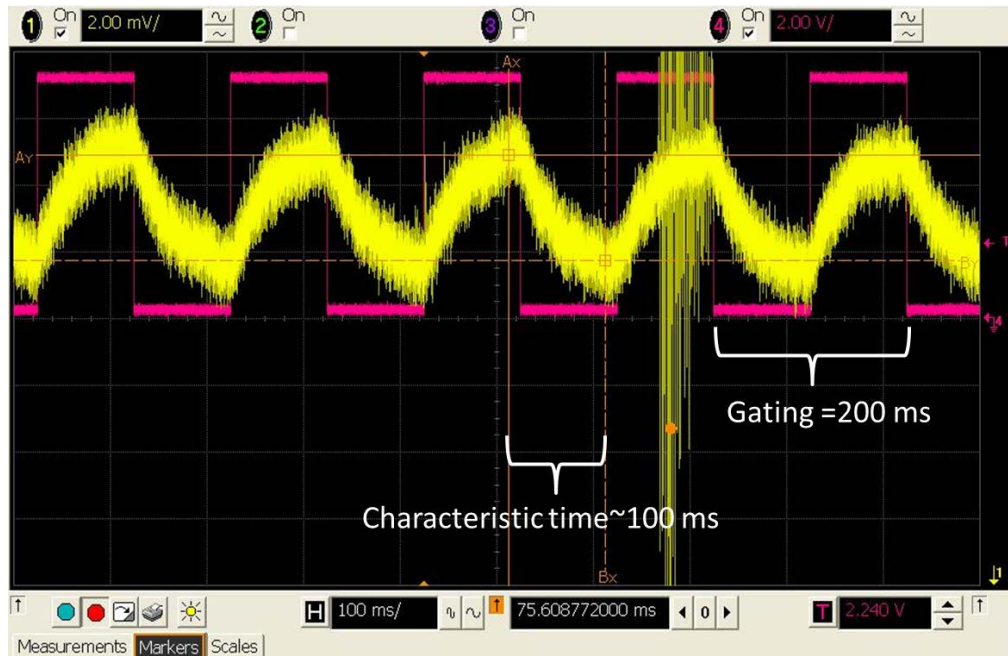

Figure 30.   Measurement of characteristic time of pyroelectric detector.

In Figure 30, both the raw detector output (yellow trace) and the triggering gate (pink trace) are shown. The pyroelectric detector has a rise time, or response from 10 percentto 90 percent of maximum, of ~100 ms. Due to this long time constant the optimum chopping frequency for the detector is approximately 5 Hz. At a faster frequency the output power of the detector will not be maximized. For the same input power, the power measured with the lock-in amplifier from the detector being chopped at 5 Hz was 1.5 times greater than the power measured with the beam being chopped at 10 Hz. A slower chopper rate would allow a slightly larger signal to be measured but the

optical chopper that will be used in the experiment for the Niowave FEL is not stable below 4 Hz which caused problems for the lock-in amplifier. For this reason, 5 Hz chopping frequency was chosen for the experiment.

To test the lock-in amplifier (LIA) a large signal was input that was measurable by the raw signal of the detector.
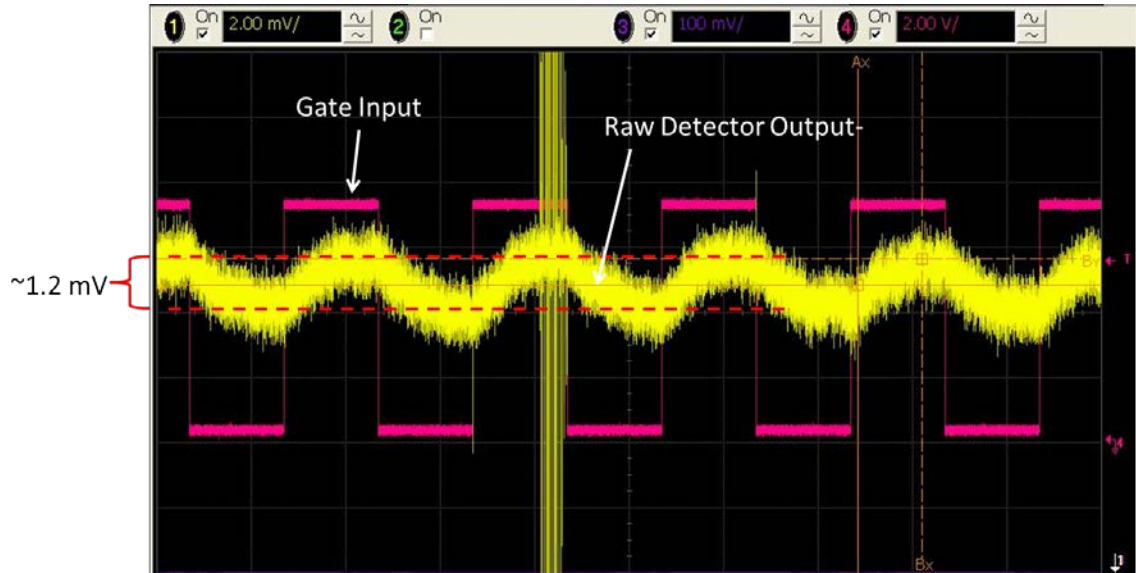

Figure 31.   Raw signal from pyroelectric detector.

Figure 31 shows the raw signal from the detector that measures a modulated THz source. Visible is the ~1 mV noise that overlays the signal. With the noise the peak-to-peak voltage of the detector signal can be roughly approximated as 1.2 mV. Next, the raw output of the detector and the gate input shown in Figure 31 was input into the LIA and the DC output examined.
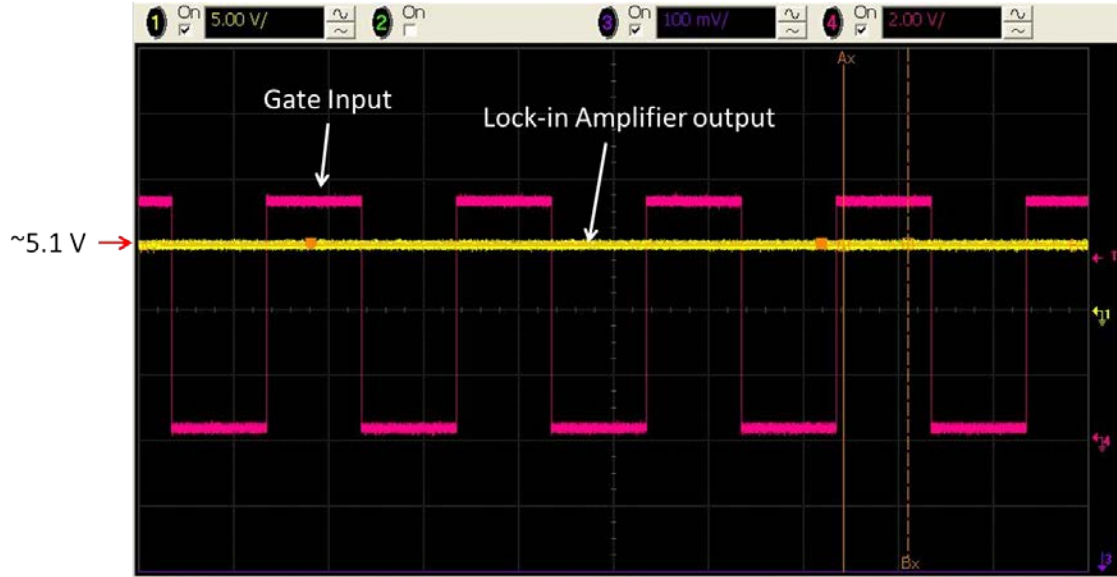
Figure 32.   Signal from lock-in amplifier (LIA)

In Figure 32, the ~5.1 V DC signal from the LIA is shown. The output from the LIA is dependent on several settings. The relationship between the output of the LIA and the raw signal can be seen in Eq. (5-5)

$$V_{out} = 10 \cdot A_e(A_v \cdot V_i \cdot \cos(\theta) + V_{os}) \,, \qquad (5\text{-}5)$$

where V_{out} is the voltage output of the LIA, A_e is the expand function (1 in this case), A_v is equal to the inverse of the sensitivity setting of the LIA (equal to 1000 V^{-1} in this case), V_i is the input voltage, θ is the phase offset between the input and reference signal (0 in this case), and V_{os} is the offset voltage (0 in this case). This calculation leads to V_i= 510 µV. This value is half of what was measured in Figure 31 as the LIA displays the magnitude not the peak-to-peak voltage.

Next, to characterize the minimum signal that could be detected with the aid of the LIA, a signal smaller than the intrinsic noise of the detector was input into the pyroelectric detector. The raw output from the detector is seen in Figure 33.
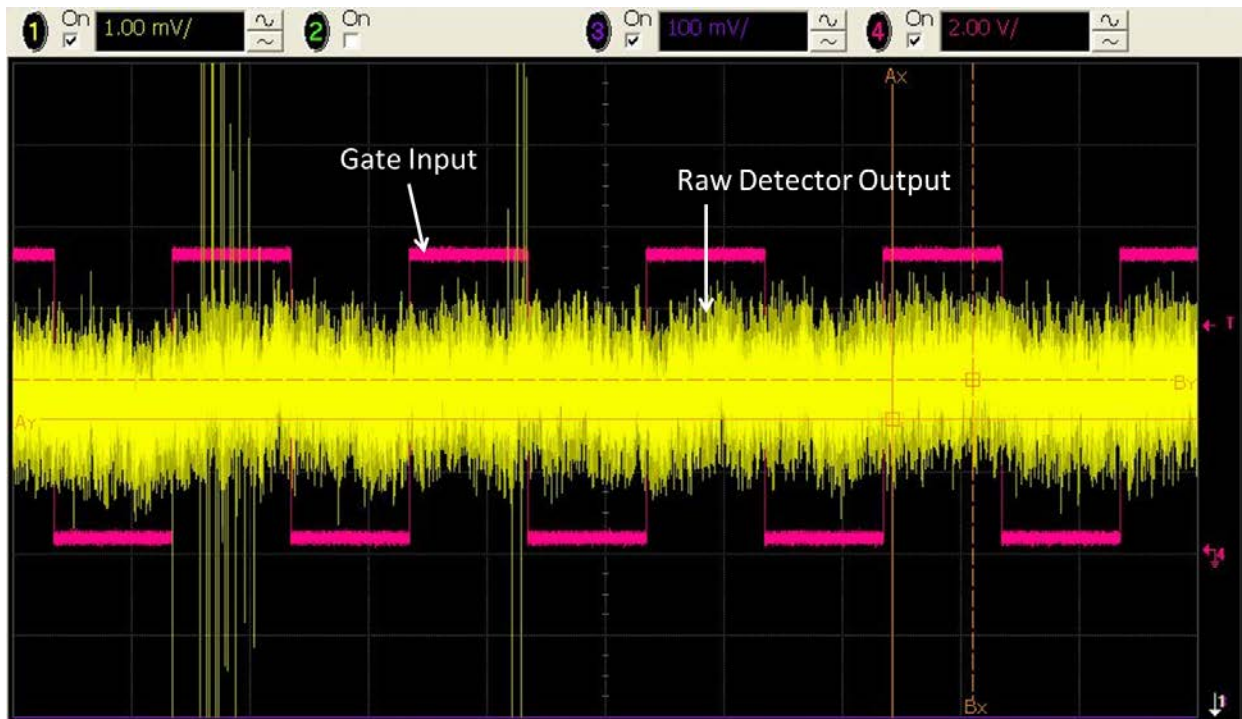
44

Figure 33.   Raw signal from the pyroelectric detector with low power.

It is self-evident that any information about the power into the detector is lost in the noise. With the use of the LIA a DC signal of 6.4 µV ±1µV was measured. With the nominal 1000 V/W sensitivity of the detector this corresponds to an input signal of ~6.4 nW ± 1 nW of power. This gives a baseline that the use of the pyroelectric detector and a lock-in amplifier will be able to measure, and is orders of magnitude smaller than the anticipated output of the FEL in the worst case scenario laid out in Table 1-1 (~4 µW).

THIS PAGE INTENTIONALLY LEFT BLANK

VI. CONCLUSION

In this thesis a beam transport path and diagnostic setup was studied and designed for the Niowave Super-radiant THz FEL. A long transport path was designed to transfer the radiation from the FEL to a diagnostic station outside the vault in a way that minimizes power loss as well as maintains spectral information of the radiation. For short distance propagation, where the spectral information is not a requirement, a light pipe transport system was designed and built to allow assessment of the Niowave FEL. A diagnostic station with a pyroelectric detector, optical chopper, and lock-in amplifier was assembled and tested to show that low power levels are measurable. Power levels as low as 6 nW were measurable which is below the worst case scenario of the Niowave FEL.

THIS PAGE INTENTIONALLY LEFT BLANK

LIST OF REFERENCES

[1]   M. Kelly, "Superconducting spoke cavities," in *High Intensity High Brightness Hadron Beams*, Tsukuba, Japan, 2006.

[2]   J. R. Delayen, C. S. Hopper, and R. G. Olave, "Design of low-frequency superconducting spoke cavities," in *Proceedings of IPAC2011*, San Sebastian, Spain, 2011.

[3]   W. B. Colson, *THz window & Transport at Lower THz Frequencies,* Monterey: Unpublished, 2013.

[4]   Z. C. Rosen et al., *Piezoelectricity*, New York: American Institute of Physics, 1992.

[5]   J. G. Webster, *The Measurement, Instrumentation, and Sensors Handbook*, Boca Raton, Fla: CRC Press in cooperation with IEEE Press, 1999.

[6]   D. F. Santavicca, "Conceptual schematic of a bolometer," Wikipedia, [Online]. Available: http://en.wikipedia.org/wiki/File:Bolometer_conceptual_schematic.svg. [Accessed 19 August 2013].

[7]   J. J. Mares, P. Hubik, M. Nesladek, D. Kindl and J. Kristofik, "Weak localization—Precursor of unconventional superconductivity in nanocrystalline boron-doped diamond," *Diamond & Related Materials,* vol. 15, no. 11–12, pp. 1863–1867, Nov.–Dec. 2006.

[8]   G. B. Armen, "Univerisity of Tennessee Physics Dept.," 2008. [Online]. Available: http://www.phys.utk.edu/labs/modphys/lock-in%20amplifier%20experiment.pdf. [Accessed 10 July 2013].

[9]   Stanford Research Systems, Inc., "Model SR450 optical chopper," 1997. [Online]. Available: http://www.thinksrs.com/downloads/PDFs/Manuals/SR540m.pdf. [Accessed 2 June 2013].

[10]   Microtech Instruments, Inc., "Microtech Instruments, Inc. THz Lenses & Windows," 2005. [Online]. Available: http://www.mtinstruments.com/downloads/THz%20Lenses%20and%20Windows%20Datasheet.pdf. [Accessed 13 July 2013].

[11]   F. L. Pedrotti and L. S. Pedrotti, *Introduction to Optics*. Englewood Cliffs, NJ: Prentice-Hall, Inc., 1993.

[12]   E. Hecht and A. Zajac, *Optics*. New York: Addison-Wesley Publishing Company, 1974.

[13]   R. Swent, private conversation. May 2013.

[14]   Precision Photonics, "Advanced design of etalons," 2013. [Online]. Available: http://www.precisionphotonics.com/technology/EtalonAdvanced.pdf. [Accessed 16 August 2013].

[15]   J. A. Stratton, *Electromagnetic Theory*, New York: Mcgraw-Hill Book Company, Inc., 1941.

[16]   R. C. Ohlmann, P. L. Richards and M. Tinkham, "Far infrared transmission through metal light pipes," *Journal of the Optical Society of America,* vol. 48, no. 8, pp. 531–533, Aug. 1958.

[17]   W. T. Welford and R. Winston, *The Optics of Nonimaging Concentrators: Light and Solar Energy*, New York, New York: Academic Press, Inc., 1978.

[18]   A. Danylov, "THz laboratory measurements of atmospheric absorption between 6% and 52% relative humidity," September 2006. [Online]. Available: http://www.uml.edu/docs/UML_STL_WaterVaporSept2006_tcm18-42128.pdf. [Accessed 17 August 2013].

[19]   P. R. Griffiths and J. A. de Haseth, *Fourier Transform Infrared Spectrometry*, Hoboken, NJ: John Wiley & Sons, 2007.

[20]   E. D. Palik, *Handbook of Optical Constants of Solids*, Orlando, FL: Academic Press, Inc., 1985.

[21]   R. Ulrich, T. J. Bridges and M. A. Pollack, "Variable Metal Mesh Coupler for Far Infrared Lasers," *Applied Optics,* vol. 9, no. 11, pp. 2511–2516, Nov. 1970.

[22]   R. Ulrich, "Far-Infrared Properties of Metallic Mesh and its Complementary Structure," *Inrared Physics,* vol. 7, no. 1, pp. 37–55, Mar. 1967.

[23]   S. Grey, "Novel Out-coupling techniques for Terahertz Free Electron Lasers," M.S. thesis, Phys. Dept. Naval Postgraduate School, Monterey, CA, 2012.

[24]   Microtech Instruments, Inc., "Pyroelectric Detector DataSheet," 2005. [Online]. Available: http://www.mtinstruments.com/downloads/Pyroelectric%20Detector%20Datasheet.pdf. [Accessed 15 April 2013].

INITIAL DISTRIBUTION LIST

1. Defense Technical Information Center
   Ft. Belvoir, Virginia

2. Dudley Knox Library
   Naval Postgraduate School
   Monterey, California